Check for updates

A time-space window between Eocene karst bauxite genesis and the first molasse deposition in the Dinaric Foreland Basin in the North Dalmatia, Croatia

Vlatko Brčić[1]*, István Dunkl[2], Andrea Mindszenty[3], Mihovil Brlek[1], Nina Trinajstić[1], Petra Bajo[4], Blanca Bauluz[5], Ivan Mišur[1], Volker Karius[2], Sanja Šuica[6], Duje Kukoč[1], Alfonso Yuste[5], Elisa Laita[5], Hilmar Von Eynatten[2] and Armin Zeh[7]

[1]Department of Geology, Croatian Geological Survey, Zagreb, Croatia, [2]Department of Sedimentology and Environmental Geology, Geoscience Centre, Georg-August-University Göttingen, Göttingen, Germany, [3]Department of Physical and Applied Geology, Eötvös Loránd University, Budapest, Hungary, [4]Department of Mineral Resources, Croatian Geological Survey, Zagreb, Croatia, [5]Departamento de Ciencias de la Tierra, IUCA-Universidad de Zaragoza, Zaragoza, Spain, [6]INA-Industrija Nafte d.d., Exploration and Production Laboratory, Zagreb, Croatia, [7]Karlsruher Institut für Technologie, Institut für Angewandte Geowissenschaften—Mineralogie und Petrologie, Karlsruhe, Germany

Karst bauxite deposits in the North Dalmatian piggyback basin (NDPGB) are a part of the Mediterranean bauxite belt, which is the largest European bauxite deposit zone; however, there is a general lack of information regarding the genesis, age, and precursor of the bauxite deposits in this region. In this study, we combined detrital zircon U−Pb geochronology with compositional, mineralogical, and morphological data from four bauxite locations in the NDPGB to provide a new palaeogeographical and palaeoenvironmental evolution model for the Lutetian−Rupelian timeframe of the NDPGB. The Eocene climatic conditions began with the Palaeocene−Eocene Thermal Maximum event (~56 Ma), followed by the Early Eocene Climatic Optimum (~49 Ma) and Middle Eocene Climatic Optimum (~40 Ma), and were completed as a cooling trend culminating around the Eocene/Oligocene boundary (~34 Ma), with a shift towards an icehouse climate. These events were coeval with the continuous drift of the African continent towards Eurasia and the subsequent closure of the western part of the former Neo-Tethys Ocean associated with massive volcanic activity. Based on the bauxite deposits of the NDPGB, Early Eocene limestones formed in the last phase of the long-lasting Adriatic Carbonate Platform. The Middle Eocene orogenic activity resulted in an elevation in this area. High average temperatures, accelerated hydrological cycles and precipitation, and intensive continental weathering with increased volcanic carbon input resulted in favourable conditions for the development of karst bauxites at this time. Further Upper Eocene tectonic deformation of the NDPGB area resulted in the development of bauxite traps and enabled redeposition of the initial bauxite material. Subsequently, the bauxite deposits were covered with clastic carbonate molasse derived from the intensive erosion of the young Dinaric orogeny. The implications of this study are as follows. First, it provides new information on the timing of bauxitisation in the area by providing the first radiometric zircon geochronology, which refined and restricted the time

window for bauxite formation in this region. Additionally, our results provide a new perspective on the possibility of aeolian precursors in karst bauxite formation and provide new constraints on the first tectonic marks of the initial Dinaric orogeny.
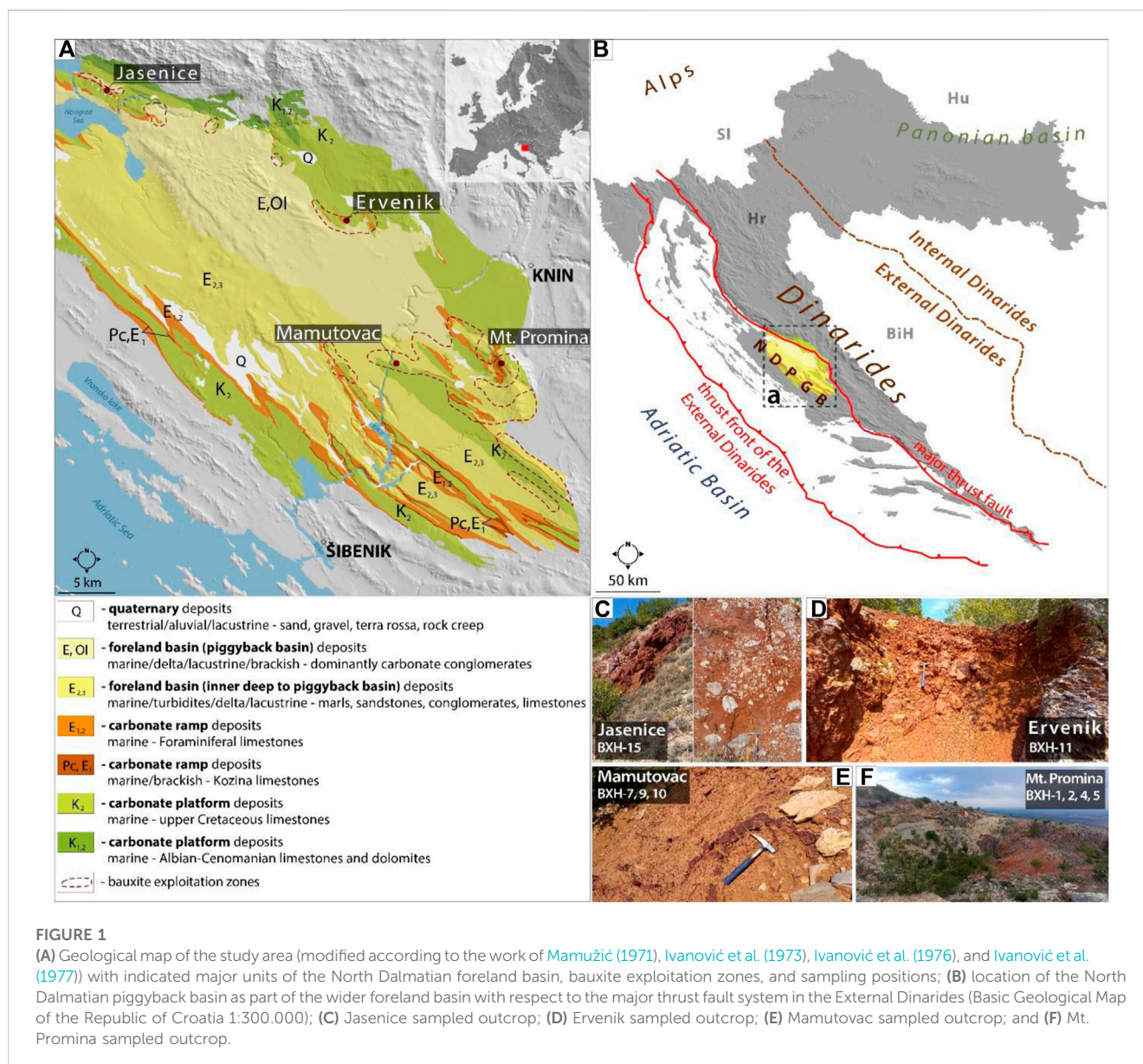
1 Introduction

Mediterranean belt karst bauxites from the aspect of their source material and genesis still represent a debated issue (Comer et al., 1980a; Šušnjara and Šćavničar, 1978; D'Argenio and Mindszenty, 1991; D'Argenio and Mindszenty., 1992; D'Argenio and Mindszenty, 1995; Sakač and Šinkovec, 1991; Yuste et al., 2015; Mindszenty, 2016; Brlek et al., 2021). By definition, bauxites are chemically weathered residual deposits enriched in Al by removing other components under hot and humid tropical and subtropical climatic conditions. The major components are Al hydroxides (gibbsite and boehmite), phyllosilicates (mainly kaolinite), iron (Fe) oxides (haematite and magnetite), Fe hydroxides (goethite), and Ti oxides (Bárdossy, 1982; Schellmann, 1994; D'Argenio and Mindszenty, 1995; Bárdossy and Combes, 1999; Retallack, 2010; Boni et al., 2013; Mongelli et al., 2014; Mongelli et al. 2016; Mongelli et al. 2017; Mindszenty, 2016; Sinisi, 2018). In terrestrial depositional settings, all argillaceous residual sediments, such as bauxite, terra rossa, or kaolin deposits, are formed as a result of discontinuous sediment accumulation and concomitant subaerial weathering (Kelemen et al., 2022; Kelemen et al., 2023). Weathering, a result of the interaction of the atmosphere and biosphere with the lithosphere, depends on tectogenesis and morphogenesis and is finally manifested as *bauxitisation cycles*. Regional cycles can be triggered by monotonous and flat or (on carbonate terrains) deeply karstified relief, greenhouse conditions, and development of an initial lateritic/ferrallitic blanket with chemical and physical degradation processes (Boulange, 1984; Valeton, 1991; Valeton, 1994). Bauxites are reliable continental palaeoclimate indicators; however, because of their "condensed" nature and the relatively long (>1 Ma) duration necessary for commercial-grade deposits formation, they are able to record only low-frequency climate changes. Thus, they can be successfully used for the reconstruction of past climatic conditions, such as long-lasting humid tropical environments and/or their change to more arid or less hot conditions. Palaeoclimatic and palaeoenvironmental conditions favourable for *in situ* bauxitization are estimated as mean annual temperatures >17°C–22°C and mean annual precipitation >1,100–1,200 mm (Bárdossy, 1982; Bárdossy and Combes, 1999; Retallack, 2008; 2010; Bogatyrev et al., 2009; Mondillo et al., 2011). Some researchers have also proposed additional restrictions that need to be fulfilled, such as less than 4 months per year of the dry season and mean atmospheric relative humidity >80% (Tardy et al., 1991). Of all known bauxite deposits in the world, 14% belong to the group of karst bauxites (Bárdossy, 1982). According to the work of Yang et al. (2022), bauxite deposits represent only <12% of the global reserves. Most of Europe's bauxite deposits are located on the northern shores of the Mediterranean (Mediterranean bauxite province). Bauxite and laterite formations

are globally unevenly distributed over time and are coeval with global events such as massive volcanic eruptions, high-temperature and -precipitation periods, CO_2 greenhouse events, release of methane hydrates from the oceans, and oceanic anoxia (Retallack, 2010; Iqbal et al., 2023). The PETM (Kennett and Stott, 1991; Zachos et al., 1993; Bralower et al., 1995; Thomas and Shackleton, 1996) represents the initiating event of the long-term highest global temperatures of the Cenozoic Era (lasting ~56–33.9 Ma and terminated by the Eocene–Oligocene transition) (Coxall and Pearson, 2007; Hutchinson et al., 2021). The most intensive Eocene bauxitisation events were dated approximately as 48 and 35 Ma (Retallack, 2009; Retallack, 2010).

This study aimed to provide new chronological constraints on the emergence phase during the Eocene in the north-eastern part of the Mediterranean bauxite belt, more precisely in the North Dalmatian piggyback basin (NDPGB). Due to the general lack of biostratigraphic data in terrestrial residual sediments such as bauxites, detrital geochronology was used to obtain the depositional ages. Detrital zircons as ultra-stable and datable minerals originating from various source rocks can be redeposited in bauxite, including volcanic/aeolian input, and may potentially constrain the maximum depositional age; this, combined with the dating of overlying deposits, results in better bracketing of a time window for the bauxitization processes (Comer et al., 1980a; Dunkl, 1992; Gehrels, 2014; Marchand et al., 2021; Kelemen et al., 2023).

Theoretically, the maximum time window between the bedrock of bauxites (foraminiferal limestones) (Ćosović et al., 2004) and the overlying molasse (Promina unit) (Babić and Zupanič, 1983; Babić and Zupanič, 1988; Mrinjek, 1993a; Mrinjek, 1993b; Babić and Zupanič, 2008; Zupanič and Babić, 2011; Babić and Zupanič, 2012; Mrinjek et al., 2012; Babić and Zupanič, 2016) stretches from the Ypresian to the Rupelian (~25 Ma). The intense weathering or bauxitisation period can last from several hundred thousand to several million years (Kennett and Stott, 1991; Zachos et al., 1993; Bralower et al., 1995; D'Argenio and Mindszenty, 1995; Thomas and Shackleton, 1996; Retallack, 2009; Retallack, 2010; Brlek et al., 2021; Heller et al., 2022). Regarding the present study, the aforementioned favourable conditions could be sustained for a maximum of 10 Ma from the Early Bartonian-to-Early Rupelian time.

Nevertheless, the main contributions of this work are palaeogeographical and palaeoenvironmental reconstructions. The first overlying molasse sediment of the Promina unit (Promina mtn.) and the maximum depositional age (MDA) of the underlying bauxite (laser ablation U–Pb ages obtained from detrital zircon crystals) indicate the proximal setting of bauxite deposits regarding the orogen and its relationship to the foreland basin and the emerged land on the wedge top. Additionally, scanning electron microscopy

FIGURE 1
(A) Geological map of the study area (modified according to the work of Mamužić (1971), Ivanović et al. (1973), Ivanović et al. (1976), and Ivanović et al. (1977)) with indicated major units of the North Dalmatian foreland basin, bauxite exploitation zones, and sampling positions; **(B)** location of the North Dalmatian piggyback basin as part of the wider foreland basin with respect to the major thrust fault system in the External Dinarides (Basic Geological Map of the Republic of Croatia 1:300.000); **(C)** Jasenice sampled outcrop; **(D)** Ervenik sampled outcrop; **(E)** Mamutovac sampled outcrop; and **(F)** Mt. Promina sampled outcrop.

(SEM), energy-dispersive spectroscopy (EDS), and X-ray diffraction (XRD) data provided insights into the origin and genesis of the source material of the bauxite deposits. By defining the duration of the emersion, bauxitization window, structural and sedimentary setting, and palaeoclimatic conditions at the time of the opening of the Northern Atlantic Ocean and closing of the Neo-Tethys, we obtained an insight into the Late Eocene environment of this part of the Mediterranean bauxite belt.

2 Geological setting of the study area

The studied bauxites are located in the External (outer) Dinarides (high karst thrust sheet according to the work of Schmid et al. (2008) and Schmid et al. (2020)), in the middle of the Dalmatian southwestern part of the mountain range (Figure 1). The complete sequence is mainly composed of carbonates and ranges from the Middle Permian to Oligocene.

The dominant succession consists of deformed deposits of the Adriatic Carbonate Platform (AdCP) ranging from the Toarcian to the Eocene (Tišljar et al., 2002; Velić et al., 2002a; Velić et al. 2002b; Velić et al. 2003; Vlahović et al., 2005; Korbar, 2009 and references therein). The formation of the Dinaric orogen was a long-lasting polyphase process associated with the closing of the oceanic realm that existed between the Adria microplate and Eurasia during the Mesozoic (Schmid et al., 2008; Schmid et al., 2020). This process culminated in the Late Cretaceous-to-Early Oligocene continental collision (Handy et al., 2015; van Unen et al., 2019). Initially, collisional shortening in the Cenomanian was characterised by the formation of intraplatform basins (Jenkyns, 1991; Brčić et al., 2017; Brčić et al., 2021). Throughout the lower part of the Upper Cretaceous (Cenomanian–Santonian), AdCP successfully re-established shallow marine palaeoenvironments regardless of the occasional drowning episodes caused by an interplay of tectonic and eustatic events (Davey and Jenkyns, 1999; Korbar

et al., 2012; Brčić et al., 2017). At the end of the Cretaceous, the continental collision of the Adria with the European plate caused the uplift and emergence (1st erosional horizon) of the AdCP with the local formation of bauxites (Sakač, 1960; Sakač, 1969; Handy et al., 2015). During the rest of the Late Cretaceous and throughout most of the Palaeocene, the studied area existed as an emerged and karstified carbonate platform (Ćosović et al., 1994; Velić et al., 2002a).

The first Lower Eocene succession that covered the Cretaceous bedrock and its palaeorelief depressions is composed of a thin bed of the palustrine and marginal marine carbonates, known as Kozina deposits (Velić and Vlahović, 2009; Španiček et al., 2017). The tectonic deformation in the Early Eocene finally transformed the long-lasting AdCP into a carbonate ramp with palaeoenvironments and deposition of the foraminiferal limestones facies (Vlahović et al., 2005; Babić and Zupanič, 2016; Ćosović et al., 2018). Until the Middle Eocene, the carbonate depositional environments terminated in the research area, with subsequent deposition of flysch sequences (Pamić et al., 1998).

From the Middle Eocene to the Early Oligocene, during the period of maximum uplift of the Dinaride orogen and the advance of thrust faulting and overthrust system, a piggyback basin was formed as a part of the North Dalmatian Foreland Basin, which is part of the wider Dinaric foreland basin system (present-day imbricate-fold belt, Mamužić, 1971; Ivanović et al., 1973; Ivanović et al., 1977; Ori and Friend, 1984; Pamić et al., 1998; Figure 1). On top of the frontal part of the orogenic wedge, emerged and exposed areas were created, causing the formation of a 2nd erosional horizon and a bauxitization phase (wedge top, Déramond et al., 1993; DeCelles and Giles, 1996). Thrust and backthrust faulted wedge-top formed exposed surfaces between Dinaric orogen and the foredeep zones of the North Dalmatian foreland basin (blind-thrust anticline ridges, Ćosović et al., 2018). Simultaneously, in the distal part of the basin, deep-sea turbidities called Adriatic (or Dalmatian) flysch were deposited with the characteristics of foredeep succession. The progressive evolution of the foredeep basin is evident from the fact that the north-western parts of the Dinaric foreland flysch deposits date back to the Early Eocene (Drobne and Pavlovec, 1991; Zamagni et al., 2008), whereas Late Eocene ages have been reported from the southeast (Tari, 2002). Periodically resedimented carbonate features, such as megabeds, olistostromes, and olistoliths, recorded in siliciclastic flysch successions are the evidence of a pronounced and continuous tectonic activity (Istria, Otoničar, 2007; Petrinjak et al., 2021).

From the Late Eocene to the Early Oligocene, the study area situated at the proximal frontal part of the orogenic wedge was abundantly filled with molasse deposits with alluvial, lacustrine, deltaic, lagoonal, and shallow-marine carbonate depositional environments (Promina Formation, Babić et al., 1995). Approximately, up to 2 km thickness of these deposits resulted from the erosion of Mesozoic and Lower Eocene carbonates inside the Dinaric fold and thrust belt propagating towards the foreland (Mamužić, 1975; Ivanović et al., 1978; Babić and Zupanič, 1983; Babić and Zupanič, 1988; Mrinjek, 1993a; Mrinjek, 1993b; Babić and Zupanič, 2008; Zupanič and Babić, 2011; Babić and Zupanič, 2012; Mrinjek et al., 2012; Ćosović et al., 2018).
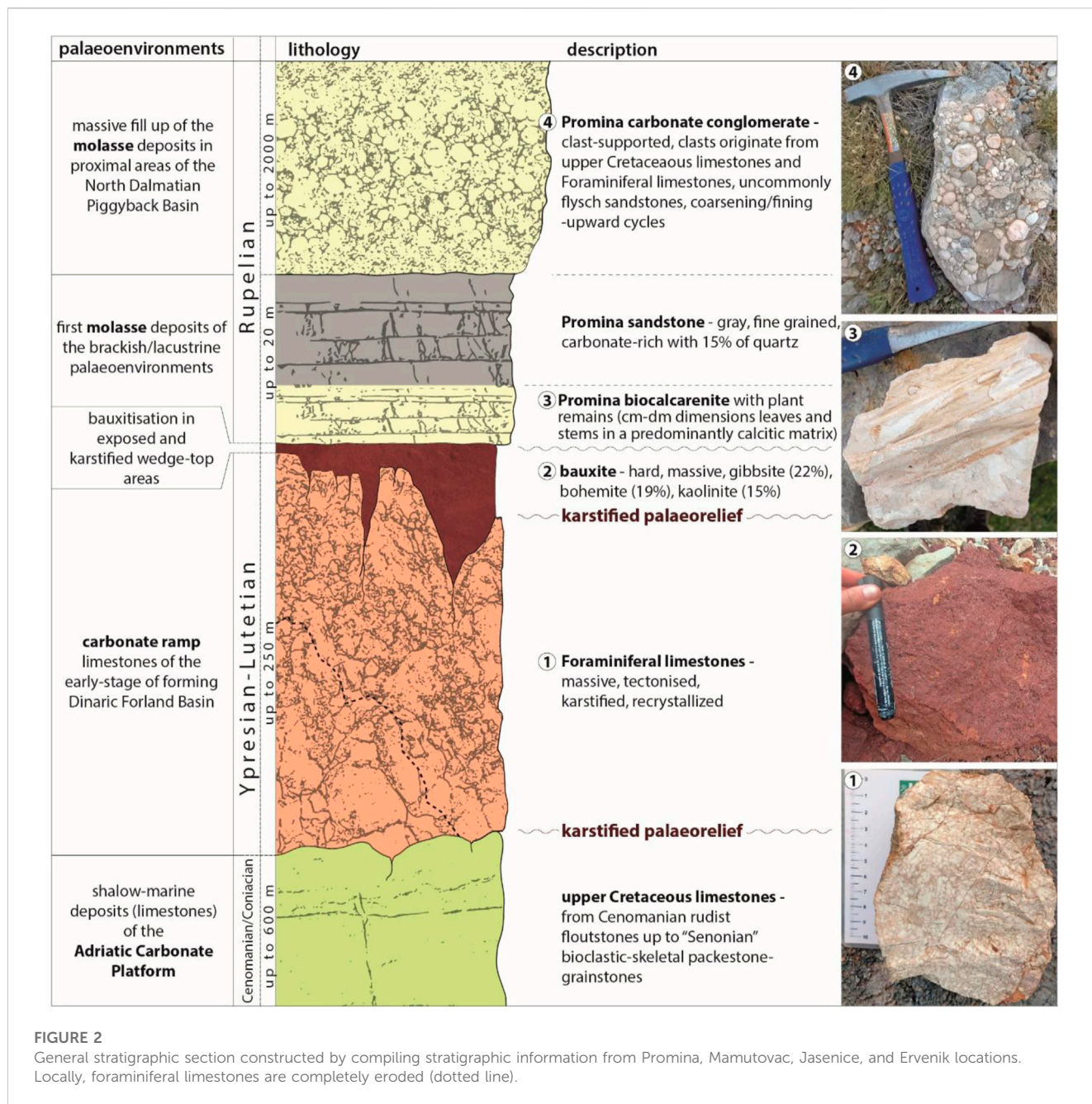
3 Materials and analytical methods

3.1 Fieldwork and sampling

In the study area (from Šibenik in the south to Knin in the north and Jasenice in the west), the most suitable exposures of karst bauxites were sampled (Figure 1). A bauxite province with an exploitation history of approximately 90 years extends in the NW–SE direction following the Dinaridic structures. The areas surrounding the selected and sampled deposits were prospectively mapped. Sampling positions were chosen in former exploitation pits, where a clear relationship between the bedrock and cover could have been established. The bauxite footwall and cover sequences were characterised by petrographic and micropalaeontological analyses to construct an integrated stratigraphic column (Figure 2). A petrographic description of the bauxite samples was obtained by optical microscopy of standard thin sections of the prevailing lithotypes (details are given in Supplementary Material). The mineralogy of the fine-grained matrix and the interior of the ooids, intraclasts, and extraclasts was examined using XRD and SEM/EDS. Carbonate rock fragments and the calcite cement were studied with a cold-stage cathodoluminoscope (MAAS-NUCLIDE, ELM-3, accelerating voltage: 6–10 kV, beam current: 0.5–0.6 mA).

Nine selected samples (eight bauxite and one biocalcarenite) from four locations (Mt. Promina, Mamutovac, Ervenik, and Jasenice) were analysed. The sampling locations are shown in Figure 1. To determine the most suitable material for further geochemical and geochronological analyses, 17 thin sections were prepared and analysed. We selected and prepared seven bauxite samples for the optical and field emission scanning electron microscopy (FE-SEM), nine for the XRD, seven for the whole-rock geochemistry, and six for the laser ablation single-collector sector-field inductively coupled plasma mass spectrometry (LA–SF–ICP–MS) zircon U–Pb geochronology (374 age data). The coordinates of the sample sites, their description, and analytical methods are listed in Table 1. The complete analytical data can be found in Supplementary Tables S1. The study materials were archived in the Croatian Geological Survey Repository.

3.2 XRD

The mineralogical compositions of all rock samples were determined by XRD analysis at the Geoscience Centre of Göttingen University, Germany. Every sample was crushed and wet-milled for 10 min in a McCrone mill using ethanol as the fluid. ZnO (10 wt%) was added as an internal standard and milled together with each sample. XRD analyses were performed on an Eigenmann GmbH Orion diffractometer (CuKα radiation 40 kV, 40 mA, primary soller slit 0.02 rad, automatic divergence slit, irradiated length 10 mm, secondary anti-scatter slit 2 mm, receiving slit 0.3 mm, Meteor E Detector). Scans were performed in the range 4°–69.5° 2θ in steps of 0.02° 2θ, 4 s counting time per step, step scan mode. The sample diameter was 20 mm, and the samples were prepared in back-loading cuvettes. Quantitative phase analyses were performed using the Rietveld method with Profex software (Döbelin and Kleeberg, 2015).

FIGURE 2
General stratigraphic section constructed by compiling stratigraphic information from Promina, Mamutovac, Jasenice, and Ervenik locations. Locally, foraminiferal limestones are completely eroded (dotted line).

3.3 FE-SEM and EDS

Thin sections were analysed using a Carl Zeiss Merlin field emission scanning electron microscope equipped with an Oxford energy-dispersive X-ray detector at the University of Zaragoza, Spain. Subsequently, thin sections were coated with carbon. Compositional images were obtained using two types of backscattered electron detectors: angular selective (AsB) and energy selective (EsB). To obtain chemical information, semi-quantitative analyses were performed by EDS with a detection limit of 0.1%. The accelerating voltage for AsB and EDS was 15 kV with a beam current of 600 pA, whereas that for EsB was 4 kV with a beam current of 1,000 pA. Morphological images of the

rock fragments were obtained using a secondary electron detector (in-lens) with an accelerating voltage of 5 kV and a beam current of 100 pA. In this case, the accelerating voltage was 5 kV, with a beam current of 800 pA.

3.4 Whole-rock geochemistry

Specimens (BXH-1, -5, -7, -9, -10, -11, and -15) were powdered using a BB-50 Retsch jaw crusher from the Croatian Geological Survey. Whole-rock geochemical data were provided by Bureau Veritas Commodities Ltd. (Canada), following standard procedures. Whole-rock chemical analysis was performed on seven bauxite

TABLE 1 Table showing name of the sample, geographical position with toponym, short outcrop description, and applied analytical methods.

Sample	Toponym	Latitude	Longitude	Lithology	Description	Analytical methods
BXH-1	Mt. Promina	N 43.92657	E 16.16159	Dark red bauxite	Side of the doline, 0.5 m above the underlying foraminiferal limestones	FESEM, EDS, XRD, whole-rock geochemistry
						LA–SF–ICP–MS zircon U–Pb geochronology, thin sections
BXH-2	Mt. Promina	N 43.92657	E 16.16159	Dark red bauxite	Side of the doline, 2.5 m above the underlying foraminiferal limestones	FESEM, EDS, XRD, thin sections
BXH-4	Mt. Promina	N 43.92657	E 16.16159	Promina biocalcarenite	Fine grained, light grey, biocalcarenite overlying on BHX-1, -2, and -5 bauxite	XRD, thin sections
BXH-5	Mt. Promina	N 43.92657	E 16.16159	Dark red bauxite	Side of the doline, 3 m below BXH-1	XRD, whole-rock geochemistry
						LA– SF–ICP–MS zircon U–Pb geochronology, thin sections
BXH-7	Mamutovac a	N 43.92998	E 16.00732	Ochre bauxite	The top part of the deposits, 0.5 m below the overlying Promina	FESEM, EDS, XRD
						Whole-rock geochemistry
						LA– SF–ICP–MS zircon U–Pb geochronology, thin sections
BXH-9	Mamutovac b1	N 43.93341	E 16.00398	Ochre bauxite	Middle to uppermost part of the deposit	FESEM, EDS, XRD
						Whole-rock geochemistry, thin sections
BXH-10	Mamutovac b2	N 43.93341	E 16.00398	Ochre bauxite	Middle to uppermost part of the deposit	FESEM, EDS, XRD
						Whole-rock geochemistry
						LA– SF–ICP–MS zircon U–Pb geochronology, thin sections
BXH-11	Ervenik	N 44.08009	E 15.91498	Ochre bauxite	North side of the doline in the uppermost part of the deposit	FESEM, EDS, XRD
						Whole-rock geochemistry
						LA– SF–ICP–MS zircon U–Pb geochronology, thin sections
BXH-15	Jasenice	N 44.2294	E 15.5729	Dark red bauxite	North side of the quarry in the uppermost part below the overlying Promina	FESEM, EDS, XRD
						Whole-rock geochemistry
						LA– SF–ICP–MS zircon U–Pb geochronology, thin sections

samples by inductively coupled plasma emission spectroscopy (ICP-ES) for major and minor elements, while trace elements, including rare earth elements, were determined by inductively coupled plasma mass spectrometry at Bureau Veritas Minerals, Vancouver, Canada. The detection limit for ICP-ES analyses was 0.01%, except for Fe_2O_3 (0.04%), whereas the detection limit for ICP–MS analysis was from 0.1 to 1 ppm.

The sample preparation procedure included melting of 0.2 g rock powder mixed with lithium metaborate/tetraborate and subsequent dissolution in aqua regia. The uncertainties in the analysis of the prepared solution by inductively coupled plasma optical emission spectroscopy (ICP-OES) for the major elements range from 0.01 to 0.002 wt%. The trace element uncertainties for the analyses by ICP–MS were assumed to be in the range of 8–0.05 ppm with the exception of gold, which has an uncertainty of 0.0005 ppm.

3.5 Zircon geochronology (LA–SF–ICP–MS)

From the bauxite samples, the zircon crystals for U–Pb geochronology were randomly selected; only inclusions and fractured areas were avoided, and no preferences were applied according to shape, colour, or cathodoluminescence (CL) intensity. Zircon crystals were fixed on a double-sided adhesive tape attached to a thick glass plate and embedded in a 25 mm-diameter epoxy mount. The crystal mounts were lapped by 2,500 mesh SiC paper and polished by 9, 3, and 1 μm diamond suspensions.

For all zircon samples and standards used in this study, CL images were obtained using a JEOL JXA 8900 electron microprobe at Geozentrum Göttingen to study their internal structures and select homogeneous parts for *in situ* age determination. The carbon coating used for CL imaging was later removed with a brief hand polish on a 1 μm diamond cloth.

The *in situ* U–Pb dating was performed using LA–SF–ICP–MS. The method employed for the analysis has been described in detail by Frei and Gerdes (2009). A Thermo Finnigan Element 2 mass spectrometer coupled with an excimer laser ablation system was used. All age data presented here were obtained by single-spot analyses with a laser beam diameter of 25 μm and a crater depth of approximately 9 μm. The laser was fired at a repetition rate of 10 Hz, and two laser pulses were used for pre-ablation. He and Ar were used as the carrier gases. Analytes ^{238}U, ^{235}U, ^{232}Th, ^{208}Pb, ^{207}Pb, ^{206}Pb, ^{204}Pb, and ^{202}Hg were measured by ICP–MS. Data reduction was based on the processing of approximately 46 selected time slices (corresponding to approximately 12 s) starting ca. 2 sec. at the beginning of a signal. If the ablation hit zones or inclusions with highly variable actinide concentrations or isotope ratios, then the integration interval was slightly resized or the analysis was discarded (~1% of the spots). Age calculation and quality control were based on drift and fractionation correction by standard sample bracketing using the GJ-1 zircon reference material (Jackson et al., 2004). For further control, Plešovice zircon (Sláma et al., 2008), 91,500 zircon (Wiedenbeck et al., 1995), FC-1 zircon (Paces and Miller, 1993), the AUSz5 (Kennedy et al., 2014), and Mud Tank zircon (Gain et al., 2019) were analysed as "secondary standards." The age results of the standards were consistently within 2σ of the published ID-TIMS values. Drift and fractionation corrections and data reduction were performed using in-house software (UranOS; Dunkl et al., 2008). The intensity of the Hg-corrected ^{204}Pb signal was very low; therefore, no common Pb correction was required. If the $^{206}Pb/^{238}U$ age was younger than 1.5 Ga, then this age was used; however, when the age was older than 1.5 Ga, then the $^{207}Pb/^{206}Pb$ age was used. This threshold value was determined empirically based on the error trends of the U–Pb and Pb–Pb ages (Spencer et al., 2016). The concordia plots and age spectra were constructed using Isoplot/Ex 3.0 (Ludwig, 2012) and Isoplot R (Vermeesch, 2018). The Shapiro–Wilk test was applied to Palaeogene ages, to determine the reliability of expressing a mean age or the necessity of searching for age components.

4 Results

During 1970–80, most deposits were partially or completely exploited. Thus, sampling at the primary position was successfully performed, considering the large number of still accessible and abandoned bauxite pits. The mapping of the bauxite bedrock and cover (determination of the underlying and overlying units) resulted in the compilation of the stratigraphic column (Figure 2). Samples BXH-1, -2, -4, and -5 were taken from the top of Mt. Promina (Figure 1) from the flanks of the open exploitation pit. The underlying unit was represented by karstified Lower Eocene foraminiferal limestones. The overlying cover unit was the Promina Formation (Upper Eocene–Oligocene molasse deposits). BXH-7, -9, and -10 belong to two bauxite pits several 100 m apart on the plateau east of the Krka River (Mamutovac; Figure 1). Unlike the Mt. Promina bauxite pit, the Mamutovac bauxite bedrock was Upper Cretaceous rudist limestone. The overlying unit was represented by deposits from the Promina Formation. The Mount Promina and Mamutovac pits are located in the eastern part of the study area (Figure 1). Sample BXH-11 was obtained from

the steep and sheared edges of an exploitation pit near Ervenik in the north-eastern part of the research area. Similar to Mamutovac, the palaeorelief bedrock consisted of Upper Cretaceous rudist limestone overlaid with the Promina Formation. Sample BXH-15 belonged to a still active quarry (former bauxite exploitation site) near Jasenice in the north-western part of the research area (Figure 1). The bedrock of the bauxite was foraminiferal limestones, and the immediate cover was unpreserved; however, there were remnants of the Promina Formation in close proximity. At all the sampled positions, the bedrock was tectonically deformed and intensely karstified.

4.1 Thin-section petrography results

Sample BXH-1 is a hard, massive, red bauxite floatstone. The matrix is pelitomorphic to microclastic, reddish to yellowish, with sepic plasmic, sometimes skelsepic, fabric (terminology in the work of Stoops et al., 2010), at places brecciated by a few strongly birefringent yellowish wispy clay seams. Scattered in the matrix, there are a few >500 μm or sometimes 2–4 mm in size, rounded, mostly dark-coloured (iron rich), and partly pale-coloured (iron poor) bauxite pebbles of various pelitomorphic or sometimes oolithic textures (Figure 3A). Their contact with the surrounding matrix was sharp. In addition to the bauxite pebbles, there was an abundance (~2.5%) of 5–10 μm-sized detrital grains and (~5–6%) of 300–400 μm-sized polycrystalline, weathered, and also, worn (possibly) silicate rock fragments (rounded to subangular, probably already transformed into crystalline) as well as tabular to subhedral gibbsite/boehmite/kaolinite. Sample BXH-2 represented a pelitomorphic/microclastic material similar to BXH-1 but was heavily impregnated with Fe oxide. Approximately, 5–10 μm-sized detrital grains occurred scattered in the sample.

Sample BXH-4 represented an immediately overlying Promina unit (top of BXH-1, -2, and -5 bauxite). BXH-4 was a reddish (limonitization of iron oxides) biocalcarenite with visible clasts smaller than 1 mm (Figure 3B). The grain size varied from 5 to 7 μm that were similar in dimension and well sorted. The siliciclastic grains were angular, whereas the carbonates were more rounded and worn. The samples were clast-to-matrix-supported. Modal analyses revealed that it consisted of fragments of monocrystalline and polycrystalline quartz, sporadic chert, plagioclase, K-feldspar, Fe-rich opaque minerals, carbonate fragments, and benthic foraminiferal bioclasts. Epidote and muscovite were identified as accessory minerals (Figure 3B). The proportion of carbonate detritus and bioclasts was approximately 70%, and siliciclastic material was approximately 30%, of which feldspar, quartz, and lithic particles were 20%, 5%, and 5%, respectively. The matrix was carbonate, micritic, or sparitic.

Sample BXH-5 was calcite impregnated with bauxite. Approximately 40% of red Fe-rich bauxite clasts/ooids were mixed with a few subangular limestone fragments and embedded in a coarse sparry calcite. Because of the strongly displaced growth of calcite, the bauxitic textural elements were detached from each other and often appeared broken. Mineral aggregates were recorded in some of the Fe oxide-encrusted bauxite grains (possibly macrocrystalline gibbsite and partly weathered, crystalline, and non-bauxitic rock fragments).
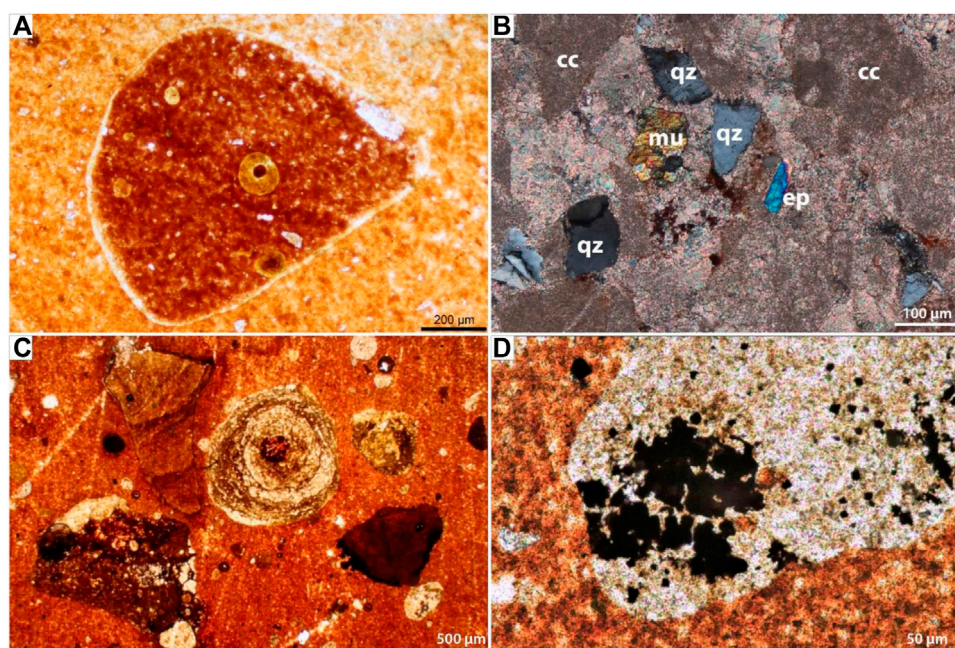
FIGURE 3
(A) Thin-section photomicrograph of sample BXH-1 (plain light) shows bauxite pebble with red, oolithic bauxite wackestone texture, embedded in lighter-coloured pelitomorphic microclastic matrix. This suggests transport and redeposition of previously lithified bauxite; **(B)** photomicrograph of sample BXH-4 with epidote (ep), muscovite (mu), quartz (qz), and carbonate clasts (cc, polarized light); **(C)** thin-section photomicrograph of sample BXH-15 (plain light) shows bauxitic wackestone with a mixed population of bauxitic clasts of various shapes, textures, and degrees of oxidation embedded in an oxidized red pelitomorphic matrix; and **(D)** thin-section photomicrograph of sample BXH-15 (plain light) shows pale coloured, rounded bauxite clast embedded in a red pelitomorphic, likewise bauxitic matrix of "aggregate" structure. The partly cubic morphology of the opaque grains in the clast points to redox conditions recorded by the clast different from those recorded by the matrix.

Sample BXH-7 (Mamutovac-a) represented oolithic bauxite from the upper part of the deposit. Approximately, 500 μm–1,000 μm-sized white ooids were embedded in the yellowish-red pelitomorphic–microclastic matrix. The nuclei of the ooids were often represented by subangular bauxite clasts surrounded by a cortex, in which the segregation of Fe-rich and Al-rich materials was sometimes observed (based on their colour; however, the ooids are overall richer in Al than in Fe). The grain size of the ooid minerals was very fine, probably the size of a boehmitic composition (both diaspore and gibbsite are known to be much more inclined to develop larger crystal sizes). Moreover, there were approximately 100–125 μm-sized scattered irregular/subangular detrital grains. Some exhibited polysynthetic twin lamellae. They might be represented by gibbsite macrocrystals, partly decomposed non-bauxitic minerals, or pseudomorphs of other non-bauxitic minerals or rock fragments. The sample was characterised by an unusual abundance of <5 μm-sized detrital grains.

The Mamutovac-b deposits contained bauxite (oolithic–intraclastic wackestone) near Fe oxide-impregnated veins. The matrix was yellowish to reddish, pelitomorphic–microclastic mudstone with pronounced *sepic plasmic*, occasionally also *skelsepic* fabric. At places, it was stained by mm-wide red–russet Fe oxide-rich stripes or by dark russet Fe oxide impregnations of irregular boundaries. Embedded in the matrix, there were pale-coloured to white ooids of 400–800 μm size, consisting of very fine-grained colourless material

showing barely visible birefringence and only occasionally having also some Fe-rich crusts. Fragments of ooids and bauxite micropebbles were also present. Almost all of these textural elements had sharp contact with the enclosing matrix. Among the embedded textural elements, a 4–5 mm-sized subangular bauxite pebble of an oolithic packstone structure was particularly conspicuous. In addition, there were several worn, partially rounded fragments of groups of crystalline Al minerals, mostly with sharp boundaries embedded in the matrix. Some were twinned macrocrystals of gibbsite or boehmite, whereas others could be fragments of reworked cavity fillings and pseudomorphs after non-bauxitic extraclasts. Moreover, there were a few scattered fine silt-sized detrital minerals (mica flakes).

The laterally sampled Mamutovac-b bauxite close to the Fe oxide-impregnated veins represented oolithic/intraclastic wackestone; however, the matrix showed abundant vague fluidal structures. The *sepic plasmic* and often *skelsepic* fabrics (characteristic of clay-rich soils) were more obvious here than in the samples aforementioned described. Larger-scale stress-related orientations of the clay-sized components of the matrix (often along microshear planes) were also observed.

Sample BXH-11 (Ervenik) represented a polymictic bauxitic wackestone/packstone. The matrix was red, Fe-rich, and pelitomorphic to microclastic or microgranular. The textural elements embedded in the matrix were (often several millimetres) bauxite pebbles and clasts of highly variegated Fe oxide content and internal texture. There were also some scattered pale-coloured ooids

TABLE 2 Semi-quantitative proportions of the mineral phases of all BXH samples.

	BXH-1	BXH-2	BXH-4	BXH-5	BXH-7	BXH-9	BXH-10	BXH-11	BXH-15
Amorph	26	22	4	8	14	10	11	2	9
Anatase	4	4	0	9	3	5	4	4	4
Boehmite	19	20	0	0	46	45	48	15	19
Calcite	0	0	74	68	0	0	0	0	0
Gibbsite	22	31	0	8	8	10	10	26	34
Goethite	4	8	0	2	10	6	7	9	8
Haematite	8	7	0	3	1	10	8	5	7
Illite	0	0	3	0	0	0	0	0	0
Kaolinite	15	5	3	0	16	12	10	15	7
Quartz	1	1	15	1	1	1	1	1	1
Rutile	1	2	1	1	1	1	1	1	1
Smectite	0	0	0	0	0	0	0	22	10

with no sign of *in situ* accretion and sharp contact with the enclosing matrix. Moreover, there were abundant (approximately 20%–25%) or sometimes several 100 μm-sized, subangular to well-rounded polycrystalline grains of gibbsite, the crystals of which were subhedral, tabular, or elongated, characterised by a birefringent 1st-order light-grey-to-yellowish colour, and often showed polysynthetic twinning. Others were fine grained and anhedral with a birefringence of 1st-order dark grey colour, such as boehmite or kaolinite.

Sample BXH-15 (Jasenice) represented oolithic/intraclastic bauxite with wackestone/floatstone textures. The matrix was reddish to yellowish, pelitomorphic (aggregated structure), and microgranular in shape. Embedded in it, there were 200–500 μm or even several mm-sized pale coloured, often broken ooids and highly variegated, partly oolithic bauxite clasts (some of them are iron oxide rich, while others, pale coloured to white, however, often with dark reddish nuclei) (Figure 3C). The quasi-concentric structure of the ooids often showed several internal discontinuities, suggesting that their formation was interrupted several times. There were also abundant worn (rounded) macrocrystals of 1st-order grey gibbsite, boehmite, and/or kaolinite. Gibbsites were identified by perfect cleavage and often visible twinning. Some of the boehmite/kaolinite crystal clusters might have been weathered fragments of plutonic or volcanic rocks.

Additionally, there are also several millimetre-sized, irregular, Fe oxide-rich clasts with an internal structure consisting of oxidised (almost opaque but reddish translucent) euhedral crystals. Some of these oxidised pseudomorphs were cubic, whereas others had rhombohedral morphologies. Small euhedral semi-oxidised pyrite crystals also occurred in pale-coloured bauxite clasts (Figure 3D). In addition to the ooids and clasts, very fine-grained unidentifiable mineral grains (some of them are mica flakes) of few μm in size and, rarely, approximately 150 μm × 200 μm-sized stubby subhedral zircon crystals could be seen scattered around the pelitomorphic matrix. No signs of *in situ* accretion were observed around any of the clasts.

4.2 XRD results

The semi-quantitative proportions of the mineral phases of all the BXH samples are shown in Table 2. Detailed data with separate diagrams are presented in Supplementary Data S1. The dominant Al-bearing phases of gibbsite, boehmite, and kaolinite were found in samples BXH-1, -2, -7, -9, -10, -11, and -15, respectively. The Fe components of these samples were haematite and goethite. Haematite was always more abundant than goethite in the presence of these Fe phases. The Ti-bearing phase in the listed samples was anatase with a smaller proportion of rutile. In sample BXH-4 and -5, the predominant phase was calcite. The only samples with a noticeable proportion of smectite were BXH-11 and -15. Quartz was present only in the BXH-4 sample (biocalcarenite).

4.3 Morphology and texture of the mineral phases (SE images) with compositional and textural backscattered electron images (BSE images)

Most of the bauxite samples (BXH-1, -2, -7, -9, -10, -11, and -15) consisted of a pelitomorphic matrix composed of nanometre-sized kaolinite, Al hydroxides (boehmite and gibbsite), goethite, and haematite. In general, kaolinite crystals were larger than Al hydroxides, although they were still nanometric and showed pseudohexagonal and anhedral morphologies (Figures 4A, B). Al hydroxides were typically anhedral and occasionally exhibited planar habits.

Samples BXH-1, -2, -11, and -15 contained both gibbsite and boehmite, which had different Al contents (34.6% and 45%, respectively). This facilitated their differentiation in EDS analyses, and they yielded different grey contrasts in the BSE images. The XRD data indicated that these samples were gibbsite-rich bauxites. The compositional images corroborated the pelitomorphic character of the bauxites, which contained variable amounts of typically
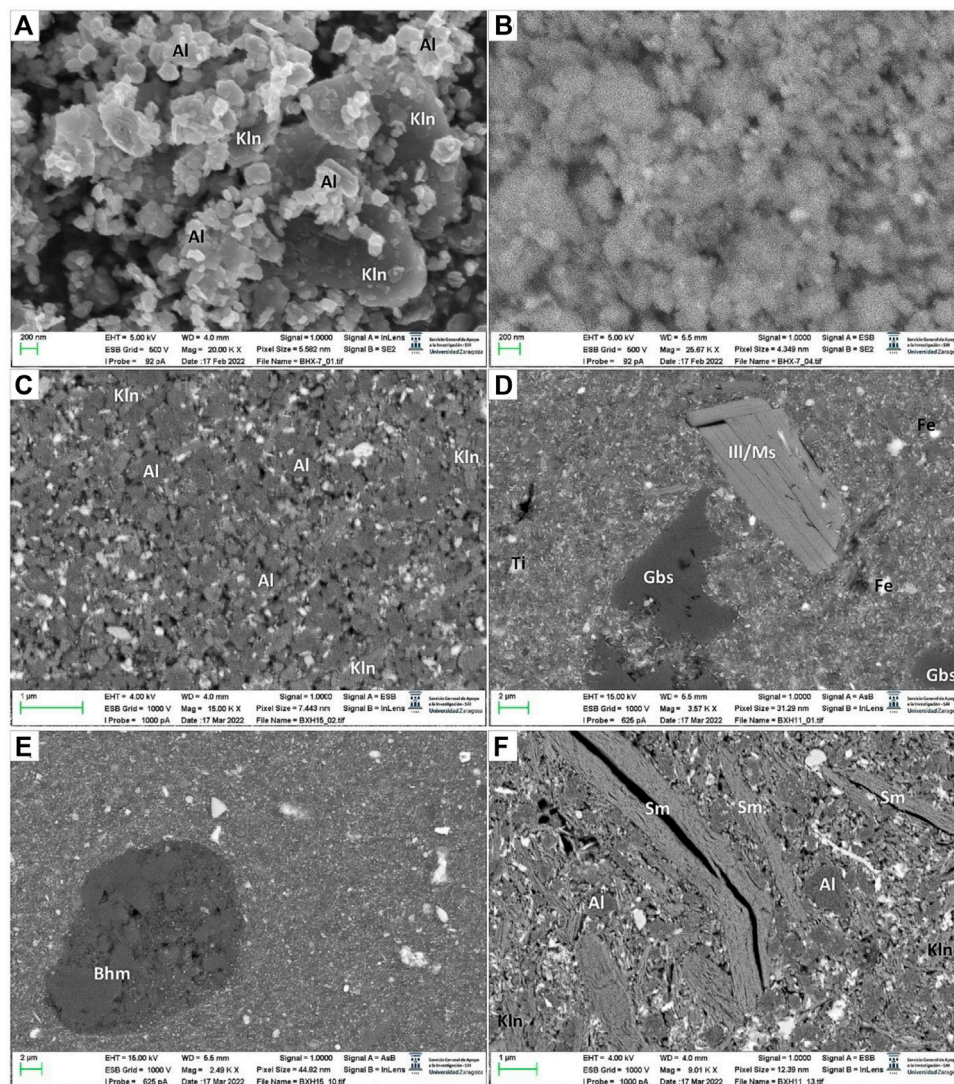
FIGURE 4
(A) Nanometre-sized, anhedral Al-oxyhydroxides, probably boehmite, following X-ray diffraction results, and nanometre-sized and larger crystals of kaolinite, occasionally showing pseudohexagonal sections; **(B)** backscattered electron image showing Fe oxides/oxyhydroxides (white grains) disseminated through the sample; **(C)** pelitomorphic matrix composed of nanometre-sized kaolinite and Al oxyhydroxides, along with disseminated Fe oxides/oxyhydroxides; **(D)** partially dissolved gibbsite. Fe and Ti oxides are also observed along with a detrital clast of muscovite/illite; **(E)** fragment of probable boehmite composed of crystals of different sizes; and **(F)** smectite aggregates embedded in the matrix composed mainly of Al oxyhydroxides, kaolinite, and Fe oxides.

anhedral nanometre-sized crystals of Al hydroxides and kaolinite (Figure 4C). Occasionally, gibbsite grains showing signs of partial dissolution were observed (Figure 4D). Boehmite fragments composed of both micro- and nanosized crystals were also observed (Figure 4E). Nanometric kaolinite "book" aggregates were occasionally observed. Additionally, anhedral, nanometric haematite, and goethite crystals could be observed scattered throughout the matrix (similar to the SE images), but detrital Ti oxide grains observed were also larger than the Fe oxides. Occasionally, up to 12 μm-sized muscovite crystals with detrital appearance, kaolinite or smectite up to 1 μm and also with detrital appearance, and several microns-large detrital smectite and kaolinite aggregates had been observed (Figures 4F, 5A). In addition to the previously described phases, embedded in the pelitomorphic matrix,

there were pisolitic bauxite rock fragments (Figure 5B), fragments of pisoids (Figure 5C), and ferruginised rock fragments or clasts (Figure 5D). In general, pisoids were heterometrical in size. They had a core and several concentric layers, although massive pisoids with no inner structures were also observed (Figure 5B). They also contained small pisoids and detrital clasts. The pisoids and ferruginised fragments were composed almost exclusively of Al hydroxides and variable amounts of Fe oxides, whereas the matrix in which they were embedded also contains kaolinite (Figure 5E). Gibbsite cement was observed within the pisolitic bauxite fragments (Figure 5F).

According to the XRD data, samples BXH-9 and BXH-10 had similar textures to those described above, although they differed from the rest of the samples in their higher boehmite content with
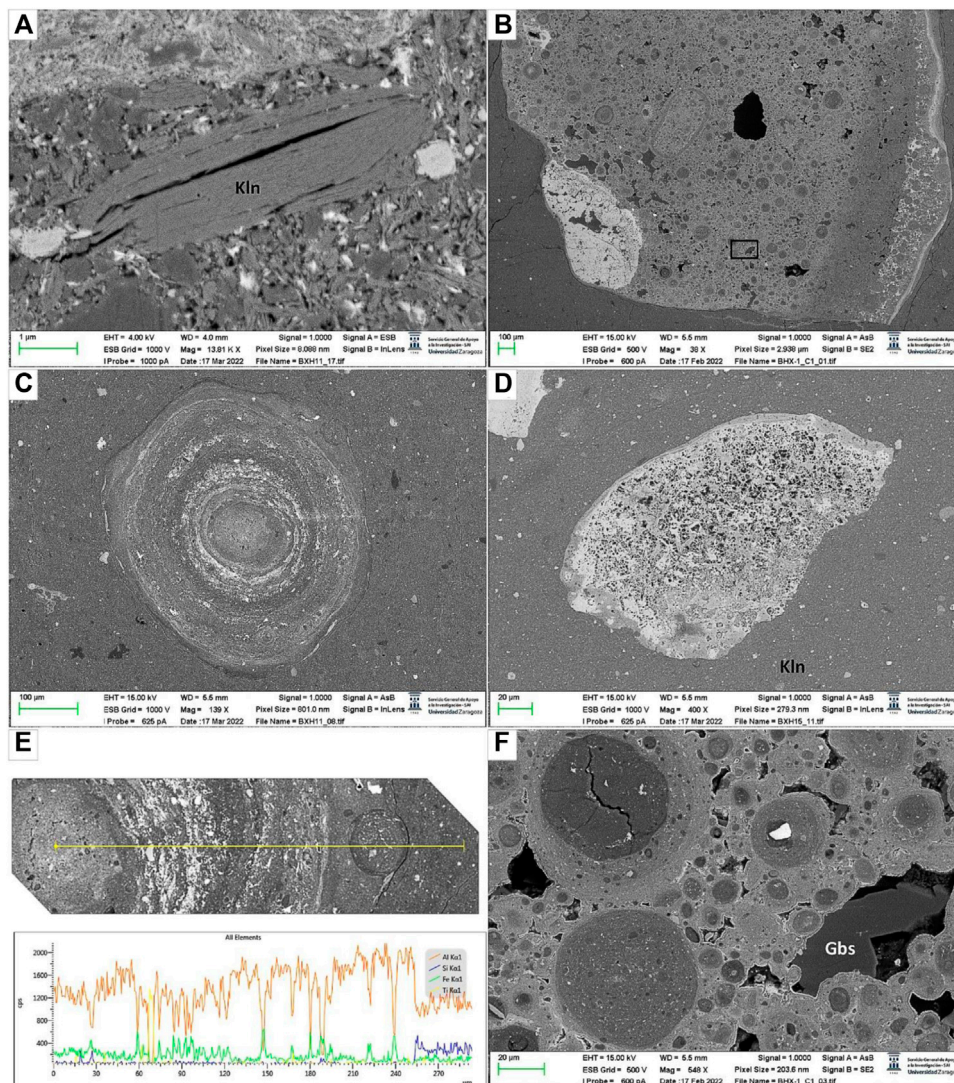
FIGURE 5
(A) Laminar kaolinite aggregate, several microns sized; **(B)** fragment of pisolitic bauxite; and **(C)** broken pisoid composed of a core and several concentric layers. A smaller micropisoid is observed included in the outermost part of the pisoid; **(D)** ferruginized rock fragment mainly composed of Al oxyhydroxides and very abundant Fe oxides/oxyhydroxides; **(E)** chemical composition from the core of the pisoid from Figure 5B to the matrix (yellow line). The matrix is richer in Si than the pisoid, indicating more abundant kaolinite. Si is very scarce in the pisoid, except for several zones in the core, probably indicating the presence of nanometre-sized detrital quartz grains; **(F)** gibbsite filling voids in the pisolitic bauxite rock fragment of Figure 5B (black square).

respect to the gibbsite content. The samples were composed of fragmented pisoids immersed in a fine-grained matrix (Figure 6). The combination of BSE images (Figure 6A) and elemental maps indicated that the cortex of the pisoids had a very high Al content but did not contain Si, suggesting the presence of Al-rich phases rather than clay minerals. The light grey contrast and Al content indicated that they were boehmites (Figure 6B). The pisoids were rich in Fe oxides and oxyhydroxides, which appeared white in the BSE images and had a high Fe content in the Fe distribution map (Figures 6C, D). The pisoids also contain a fine-grained matrix composed of Al and Si, suggesting the presence of kaolinite. Gibbsite-rich fragments were also observed (Figure 7A), which contained broken pisoids, Fe oxides, and boehmite fragments

(Figure 7B). In Figures 7C, D, boehmite partially replaced by gibbsite is clearly observed.

4.4 Whole-rock geochemistry results

The samples were qualified as bauxitic to ferritic bauxite (Figure 8A) with a high Al_2O_3 content and an average of 48.2 wt % and Fe_2O_3 19.9 wt%. SiO_2 content was different in all samples, ranging from 5.6 to 13.1 wt%. Sample BXH-5 was not included in the average because of its high carbonate content, which was visible in major element analysis where CaO was 38.0 wt%, whereas in the rest of the samples, it was approximately 0.19 wt%. The loss on
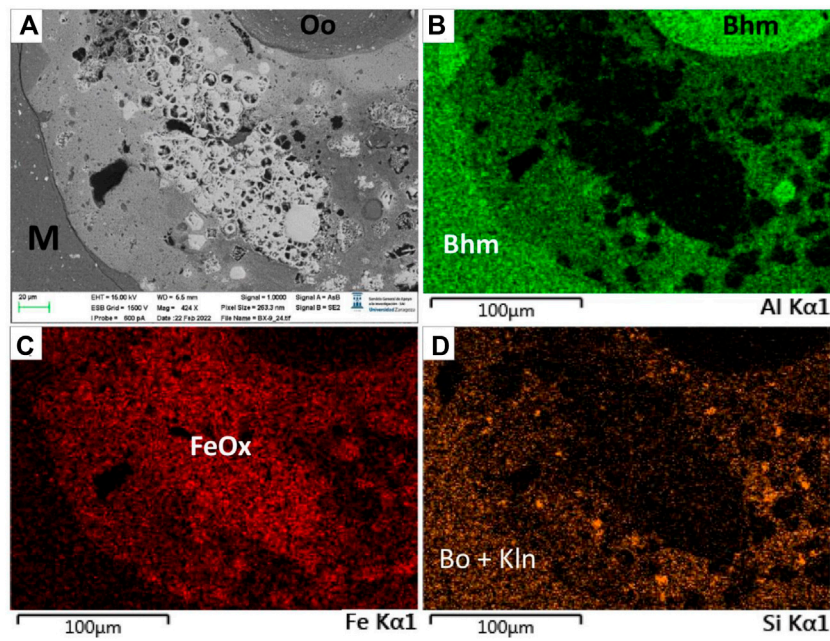
FIGURE 6
(A) Backscattered electron image and compositional maps showing the distribution of **(B)** Al, **(C)** Fe, and **(D)** Si in a rock fragment and in the fine-grained matrix. According to these maps, the rock fragment is composed of Fe oxides/oxyhydroxides and kaolinite. The matrix and a fragmented pisoid are composed mainly of boehmite.
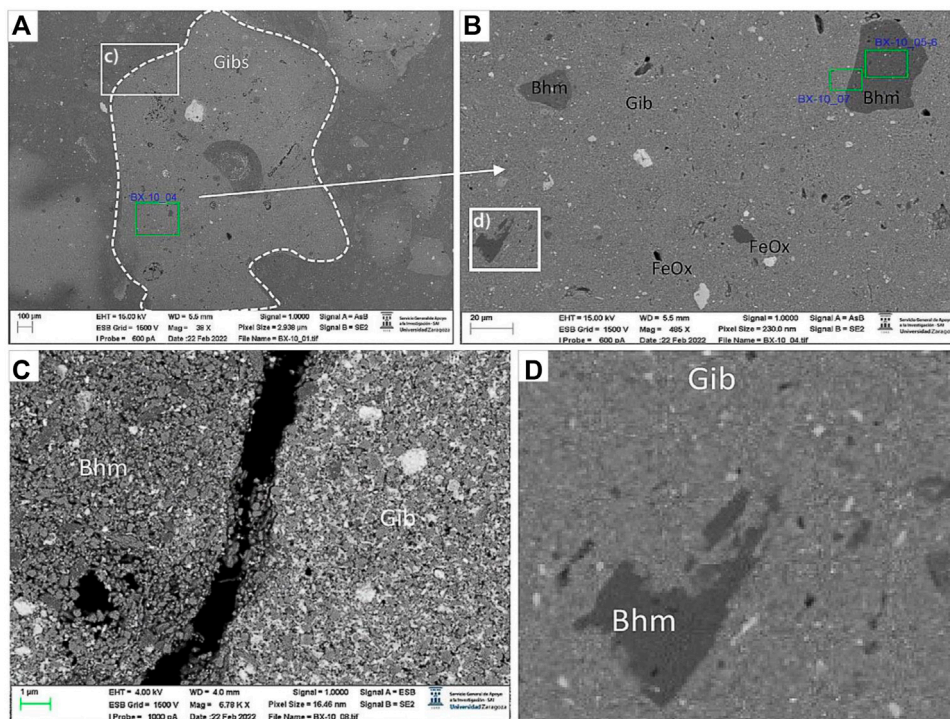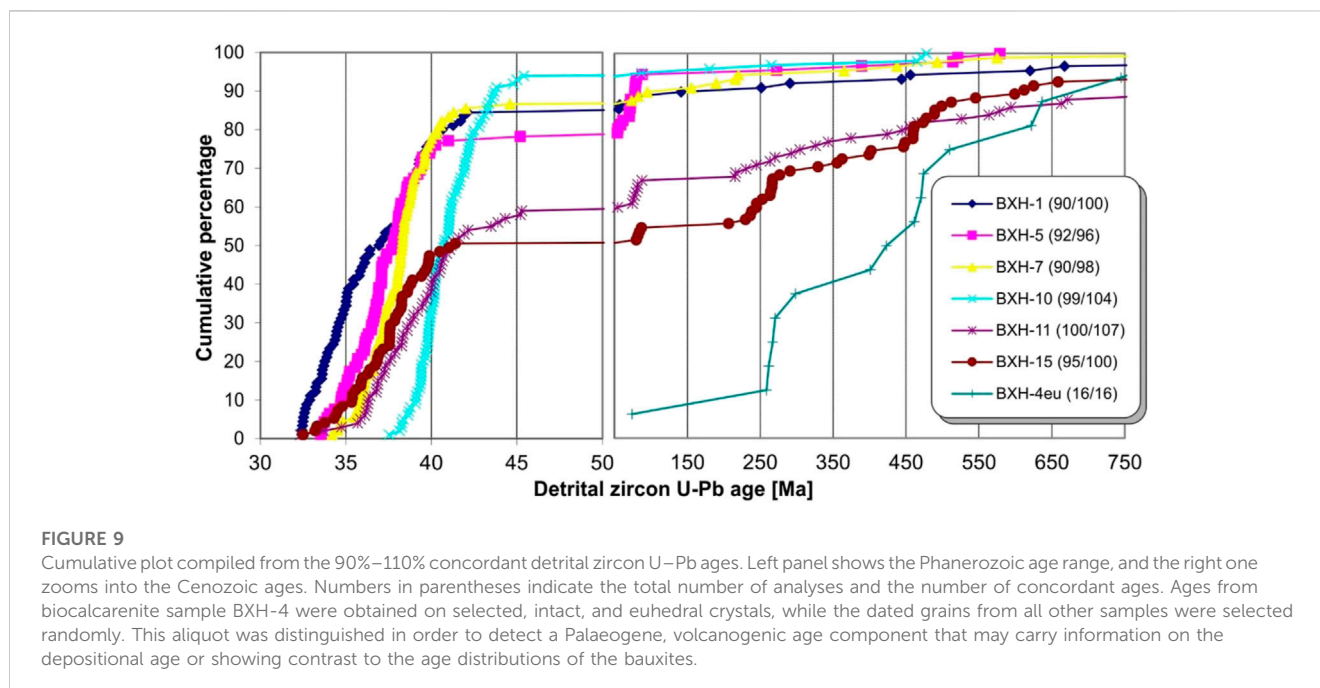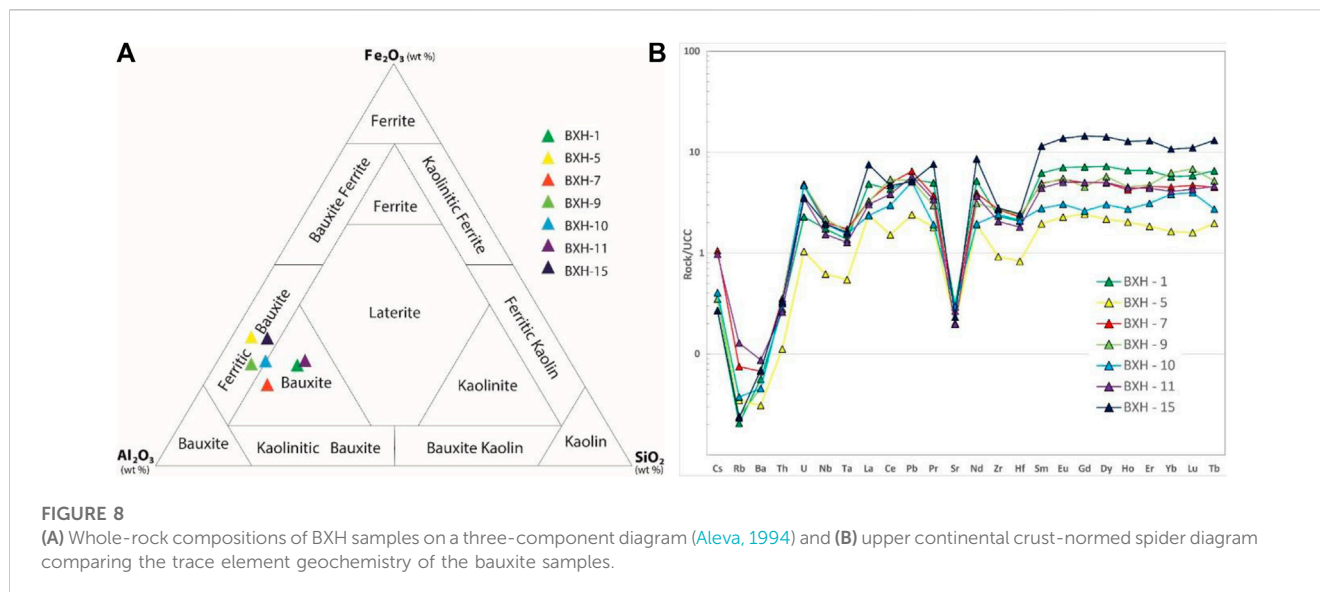

FIGURE 7
(A) Gibbsite-rich fragment composed of pisoid fragments and Fe oxides; **(B)** enlargement of **(A)** showing boehmite clasts and Fe oxides; **(C)** enlargement of **(A)** showing boehmite partially replaced by gibbsite; and **(D)** enlargement of **(B)** showing that the matrix is rich in gibbsite and the fragment is rich in boehmite.

FIGURE 8
(A) Whole-rock compositions of BXH samples on a three-component diagram (Aleva, 1994) and **(B)** upper continental crust-normed spider diagram comparing the trace element geochemistry of the bauxite samples.

FIGURE 9
Cumulative plot compiled from the 90%–110% concordant detrital zircon U–Pb ages. Left panel shows the Phanerozoic age range, and the right one zooms into the Cenozoic ages. Numbers in parentheses indicate the total number of analyses and the number of concordant ages. Ages from biocalcarenite sample BXH-4 were obtained on selected, intact, and euhedral crystals, while the dated grains from all other samples were selected randomly. This aliquot was distinguished in order to detect a Palaeogene, volcanogenic age component that may carry information on the depositional age or showing contrast to the age distributions of the bauxites.

ignition was high, with an average of approximately 18 wt%, and the highest value was in sample BXH-5 (36.8 wt%).

The rare Earth element (REE) values were normalised to upper continental crust (UCC) values using those from the work of Taylor and McLennan (1985). In this study, LREEs refer to light REEs and included REEs from La to Gd, whereas HREEs refer to heavy REEs and include REEs from Tb to Lu. The (Yb/La) UCC and (LREE/HREE) UCC ratios were calculated from values normalised to the UCC (Taylor and McLennan, 1985).

The total REE content (Supplementary Material; Figure 8B) ranged from 270 to 1,045 ppm, with the lowest values recorded in sample BXH-5. The (LREE/HREE) UCC ratio ranged from 0.89 to 1.27, with samples BXH-5 and BXH-7 showing a slight enrichment

in LREEs relative to HREEs, while in samples BXH-9, BXH-10, and BXH-15, HREEs were slightly enriched relative to LREEs.

4.5 Detrital zircon U–Pb results

The detrital zircon crystals were mostly euhedral, and their CL patterns typically showed oscillatory zoning (Supplementary Data S1). The detrital zircon U–Pb ages of the bauxite samples are divided into three major age ranges (Figure 9). Palaeozoic ages were obtained in 5%–25% of the dated grains; they formed diffuse Permian, Variscan, Ordovician, Cadomian, and Proterozoic age clusters. Their limited abundance hindered the determination of
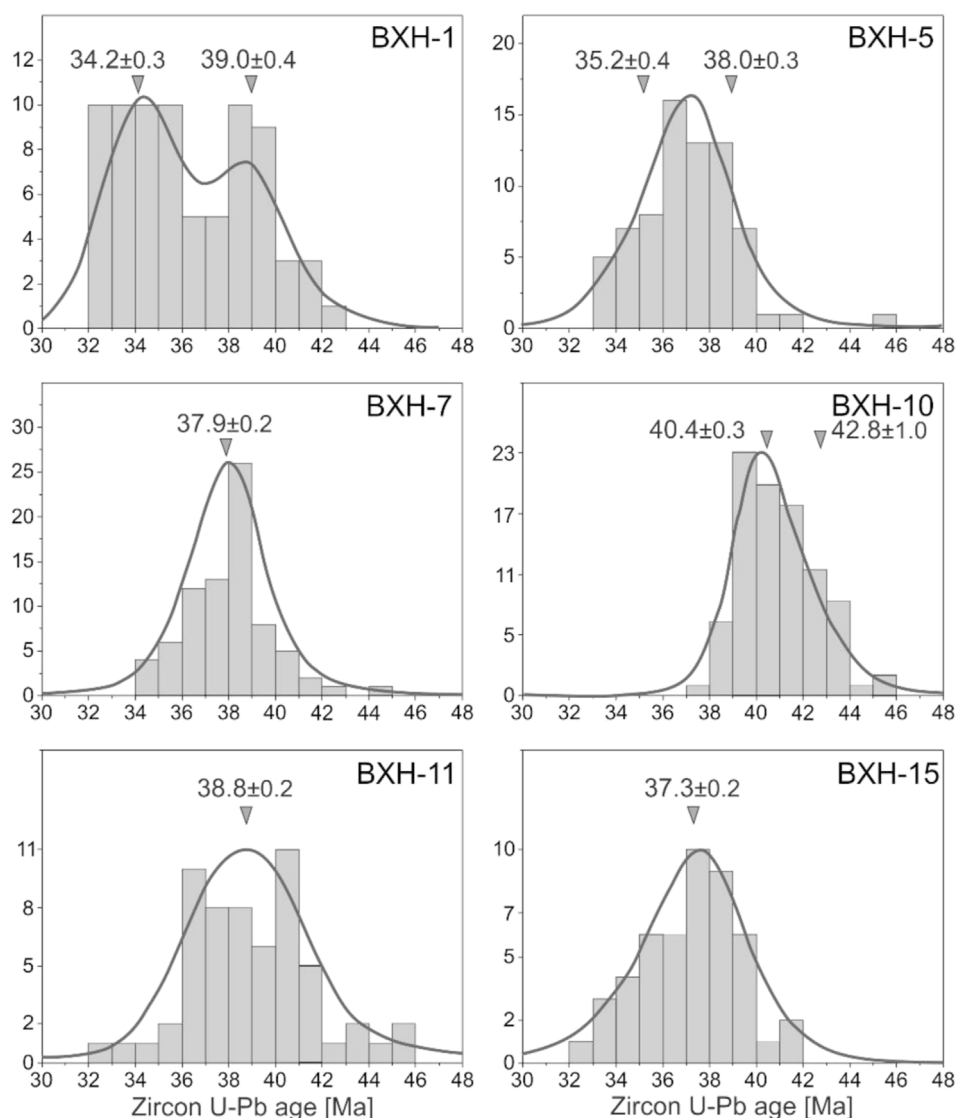
FIGURE 10
Binned plots and kernel density curves generated from the Cenozoic zircon U–Pb ages obtained in the bauxite samples. The mean and standard error of the isolated age components were determined by DensityPlotter software (Vermeesch, 2012).

highly diagnostic age components. All samples contained a few, but well-distinguishable, Late Cretaceous ages; in two samples, their amounts facilitated the calculation of mean ages of ca. 74 and 80 Ma (Age Component Table in Supplementary Data S1). Palaeogene ages form the dominant part of the age spectra, ca. 60%–90% of the data were in the range of 45 to 32 Ma. Remarkably, the samples yielded different Palaeogene ages. This was clearly visible in the cumulative plot; for example, the youngest age in sample BXH-10 was considerably older than the majority of the single-grain ages in samples BXH-1 and -5 (Figure 9, right panel). The statistical comparison of the Palaeogene age ranges by the Kolmogorov–Smirnov test showed mostly dissimilarities; only the age distributions in the two Mt. Promina samples and one Mamutovac and the Ervenik sample did not fail the test at 95% level of confidence. The Mt. Promina samples (BXH-1 and 5) failed the normality test; thus, for these data, we performed age component

identification using DensityPlotter software (Vermeesch, 2012), whereas for the other three samples, the mean ages were expressed (Figure 10, Age Component Table in Supplementary Data S1). In the Mt. Promina samples, the means of the older and the younger age components were similar, approximately 38.5 and 34.5 Ma. For samples 7, 10, and 11 with unimodal Palaeogene age distributions, we applied two methods to identify the characteristic mean ages and check their robustness. Moreover, DensityPlotter and TuffZirc used different algorithms and yielded similar mean values. Notably, the older age components in the Mt. Promina samples and in the BXH-7 and -11 samples were indistinguishable, whereas the BXH-10 sample contained a considerably older age component.

The Palaeogene ages carried the most relevant information on the ages of the tuff supply and accumulation periods of the bauxite. These volcanogenic zircons were euhedral, and their edges and tips

were completely intact. Therefore, we selected the most intact and light-coloured zircon crystals from the immediate cover sandstone of the Mt. Promina deposit to identify traces of synsedimentary volcanic activity. However, the zircon aliquot from the BXH-4 sample contained only one Cretaceous crystal, and the majority of the data were from the pre-Mesozoic (Figure 9). The Permian and older ages found in this sandstone and in the bauxite samples were very common in the detrital zircon age spectra in the basement and in the Mesozoic and Cenozoic clastic sediments of the European Alpine chain (Krippner and Bahlburg, 2012). Thus, we did not consider pre-Mesozoic ages in the interpretation of the U-Pb data.

5 Discussion

5.1 Preconditions and timing for bauxite deposit formation

During the Early Eocene, the study area was located at least 5° more to the south from its present-day position (Stampfli, 2005; Scotese, 2014). Climatic conditions around that time were generally humid and warm, characterised with a few distinctive climate optimums known as the PETM (Kennett and Stott, 1991; Koch et al., 1992; McInherney Wing, 2011), Early Eocene Climatic Optimum (EECO, ~49 Ma, Shackleton and Kennett, 1975; Zachos et al., 2001; Lear et al., 2004; Kochhann et al., 2021), and the Middle Eocene Climatic Optimum (MECO, ~40 Ma, Bohaty and Zachos, 2003; Jovane et al., 2007; Bohaty et al., 2009; Van der Boon et al., 2021; Westerhold et al., 2020). Initial warming in the Late Palaeocene accelerated the hydrological cycle, leading to intensive continental weathering and precipitation on the continents (McInherney Wing, 2011) and increased terrestrial flux into basins (Alegret et al., 2009), which resulted in a high abundance of kaolinite in weathering crusts and sediments (Gibson et al., 2000; Bauluz et al., 2014). The geologically rapid carbon release and global warming during the PETM suggest mass volcanic carbon release (Kender et al., 2021). The MECO, which lasted ~500 kyr (initiated at ~40.5 Ma and terminated at ~39.9 Ma), was also considered as having been driven by an increase in volcanic carbon input (Van der Boon et al., 2021 and references therein).

Given the duration of continuously high average temperatures in the period (~56–34 Ma) spanning from the PETM to EECO and MECO and terminating at EOT (Zachos et al., 1996; Kochhann et al., 2021), the study area must have been strongly influenced by subtropical climatic conditions (the remains of subtropical plants are found even in the overlying Eocene–Oligocene deposits dated at ~31 Ma; Figure 2). Karstification of the exposed Eocene foraminiferal and Cretaceous limestones under conditions of high mean temperatures and intense subaerial weathering led to the formation of a monotonous and flat relief characteristic of the greenhouse atmosphere, as reported by Valeton (1991, 1994) and others. This implies that climatic conditions favourable for bauxitisation (Bárdossy, 1982; Bárdossy and Combes, 1999; Retallack, 2008; 2010; Bogatyrev et al., 2009; Mondillo et al., 2011) were already fulfilled during the Lutetian, with initial bauxitisation of the source material (partly represented by volcanoclastic material) collected in the study area. According to the study of Bárdossy and Aleva (1990), Valeton (1994), and Retallack (2009, 2010), the most

pronounced bauxitisation events of the Eocene occurred at 48 and 35 Ma. Finally, all these processes and events, including tectonic deformation and geographical position, created favourable conditions for initial bauxitisation and at least partial redeposition of bauxites on limited parts of the exposed carbonate ramp (Figure 11C).

Continuous convergence between the African and Eurasian Plates and the opening of the North Atlantic in the Early Eocene (Kázmér et al., 2003; McQuarrie et al., 2003; Stampfli, 2005; Storey et al., 2007; Scotese, 2014; Metcalfe, 2021) led to a decrease and closure of the western part of the former Neo-Tethys (Allen and Armstrong, 2008; Khomsi et al., 2016; Metcalfe, 2021). Tectonic deformation transformed the long-lasting AdCP (approx. 90 Myr in the study area) into a carbonate ramp with the number of developed palaeoenvironments and the deposition of the foraminiferal limestones (Vlahović et al., 2005; Babić and Zupanič, 2016; Ćosović et al., 2018; Figures 11A–C). Furthermore, parts of the ramp emerged, and karstification of foraminiferal and Cretaceous limestones could have begun.

Eocene magmatic activity was widespread from the North Atlantic to Turkey and from North Africa to the Alps (Dal Piaz et al., 1988; Pamić et al., 2002; Lustrino et al., 2009; Marchev et al., 2013; Erturk et al., 2018; Aydınçakır et al., 2022). Volcanogenic intercalations were found in the Middle Eocene-to-Lower Oligocene strata in peri-alpine basins (Van Couvering et al., 1981; Farics et al., 2019; Ji et al., 2019). Considering that mentioned above, the time span between the Lutetian and Rupelian must have represented more than sufficient time for the emerged end eroded NDPGB palaeorelief to easily collect any of the products of the (non) mentioned episodes of the aeolian volcaniclastic material.

The present detrital zircon U–Pb ages revealed three pulses of accumulation of Eocene volcanic ash in the studied bauxite deposits at ca. 41, 38.5, and 34.5 Ma. The oldest age component detected in one of the Mamutovac samples (BXH-10) coincided with the deposition of the youngest foraminiferal limestones (Nummulitic limestones; Babić and Zupanič, 2016) forming the Palaeogene palaeorelief (Figure 2). Since the Mesozoic Adriatic Carbonate Platform was an isolated domain without continental influence (Vlahović et al., 2005), and furthermore, since the Lower Eocene carbonate ramp was characterised by deposition of the foraminiferal limestones (pure carbonate succession), volcaniclastic deposits/ tephra could be imposed as a logical choice for being one of the main precursor materials of the present-day bauxite mass. Assuming that only part of the bauxite was formed by the alteration of volcaniclastic material (Herriot et al., 2019; Sharman and Malkowski, 2020; Brlek et al., 2021) brought by aeolian transport (Boni et al., 2012; Smith et al., 2016; Yang et al., 2022; Brlek et al., 2023), the dominance of the population of dated zircons represented the lowermost stratigraphic limit of the initial Early-to-Middle Eocene bauxitisation in the NDPGB (ca. 41 Ma).

5.2 Bauxite deposit formation and development

Bauxite deposits are globally unevenly distributed and, through time, have been coeval with global events, such as massive volcanic eruptions (Yang et al., 2022), periods of high warmth and high humidity, and CO_2 greenhouse events (D'Argenio and Mindszenty,
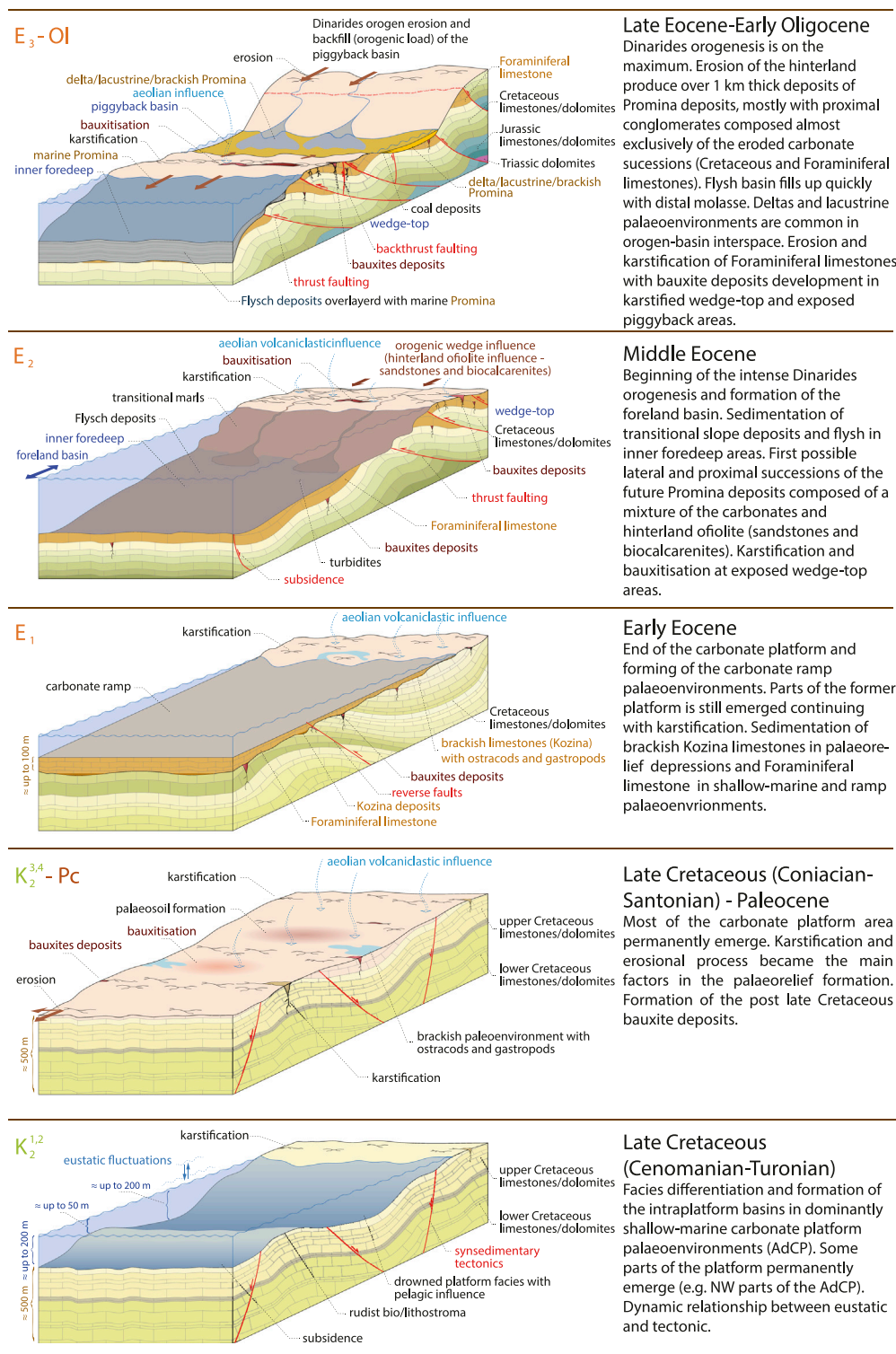
FIGURE 11
Block diagrams of the evolution and development of the large-scale study area and NDPGB with the main phases: Cenomanian-Turonian **(A)**, Coniacian-Paleocene **(B)**, Early Eocene **(C)**, Middle Eocene **(D)**, and Late Eocene-Early Oligocene **(E)**.

1995; Mindszenty, 2016). Karst bauxites in Europe are primarily situated on the northern shores of the Mediterranean Sea (Mediterranean bauxite province extending from Spain to Turkey and Iran; Bárdossy, 1982; Khosravi et al., 2017).

The trace element composition (Maksimović, 1968; Maksimović,1976; Maksimović and Pantó, 1978; Deady et al., 2016; Radusinović and Papadopoulos, 2021; Tomašić et al., 2021) and content of Zr, Ga, and Cr (Özlü, 1983; Ilijanić et al., 2023) of the
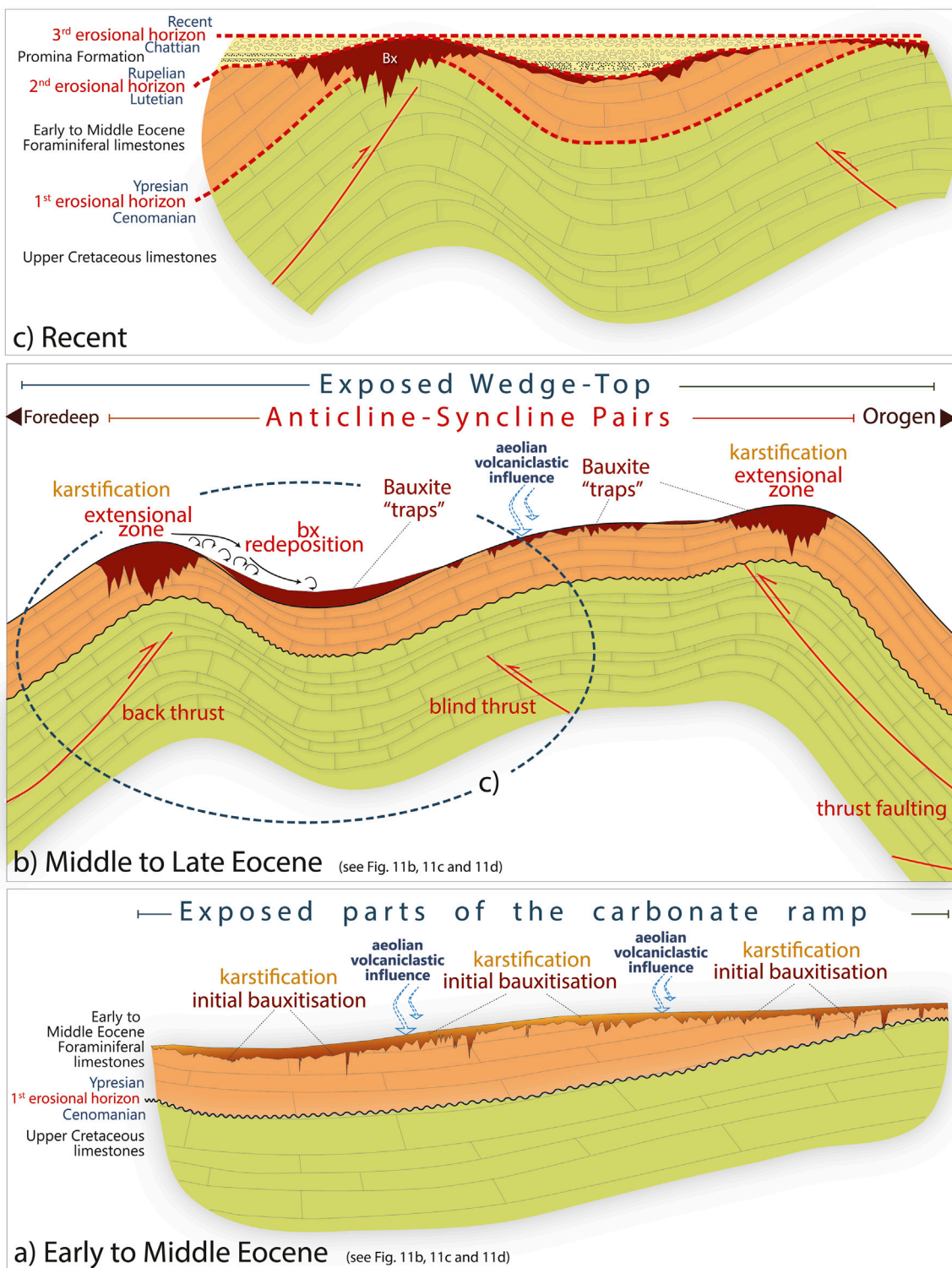
FIGURE 12
Evolution and development of the small-scale NDPGB bauxite deposits with redeposition processes and formation of the bauxite traps: Early to Middle Eocene **(A)**, Middle to Late Eocene **(B)**, and recent **(C)**.

bauxites in the Mediterranean belt show no genetic relationship with the calcareous basement. REEs become concentrated in bauxite deposits either by adsorption on the surface of clay-size constituents (Estrade et al., 2019) or by authigenic REE-bearing

minerals crystallised during bauxitisation (Deady et al., 2014). In the NDPGB bauxite samples, the total REE content ranged from 270 to 1,045 ppm (Figure 8). According to the work of Deady et al. (2014) and the references therein, the typical total REE concentrations in

karst bauxites ranged from 100 to 500 ppm. This slightly higher content could have been a consequence of multiple volcanic contributions. The processes of bauxitisation possibly influenced the original REE pattern, leading to a relatively wide range of LREE/HREE ratios (La/Yb cn from 4.8 to 13.6) in our bauxite deposits (Karadağ et al., 2009). The noticeable variation in Ce/Ce* indicates that the conditions were different in bauxite deposits. The Ce/Ce* >1 that is driven by oxidation is noticeable in BXH-7, -9, -10, and -11 (Mongelli et al., 2014; Khosravi et al., 2017), while in BXH-1, -15, and -5, the Ce/Ce* is <1. In BXH-5, bauxite concentrations of trace elements are highly depleted possibly correlative with high CaO concentrations. The Eu/Eu* ratio is considered to remain constant during bauxitisation; therefore, it can be used as a proxy for the source of the parental material (Mondillo et al., 2011; Mongelli et al., 2014). Indeed, the investigated samples displayed relatively uniform values of the Eu anomaly, with chondrite-normalised (McDonough and Sun, 1995) values of Eu/Eu* = 0.68–0.78. This was close to or slightly higher than the values for the upper continental crust (Eu/Eu* = 0.65, Taylor and McLennan, 1985) and could indicate both recycled sedimentary or felsic-intermediate volcanic origin.

Subaerially exposed parts of the Lower-to-Middle Eocene carbonate ramp was located in the hinge zones of the emerged wedge top (Figures 11, 12A, 12B). In the southern and western parts of this zone, the inner foredeep of the North Dalmatian foreland basin opened (Babić and Zupanič, 2012; Španiček et al., 2017), whereas the northern and eastern parts represented the orogenic wedge of the future Dinarides (Figure 11). The deformed foreland basin margin involves growth structures, angular unconformities, syn-depositional folding, intraformational faulting and uplift, alluvial and marine onlaps onto deformed basement, and proximal-distal variations in facies and sediment thickness (Zupanič and Babić, 2011; Ćosović et al., 2018). A gradual increase in the intensity of thrusting and faulting during the Middle Eocene formed anticline–syncline pairs on the emerged wedge top. The hinge zones exhibited extension and were prone to intense karstification. This led to the opening of deeper fracture systems and creation of potential bauxite traps. Synclinal depressions also represented potential traps, especially for bauxite redeposited from the limb zones of the anticline-syncline pairs (Figures 12B, 12C). These processes created conditions for long-term repeated re-sedimentation and diagenesis of the bauxite deposits until the Eocene–Oligocene transition and the deposition of Promina molasse, which finally covered the entire area. The youngest identified zircon age component of the NDPGB bauxite deposits is ca. 34.2 Ma (Priabonian–Rupelian transition).

The petrography of the Eocene NDPGB bauxites (bauxitic wackestones; Figures 3–6) and the observed fragments of pisolithic bauxite in the BSE images showed clear signs of allochthony. Redeposited sand-to coarse-sand-sized fragments of already lithified bauxite and allochthonous or at least parallochthonous ooids from previously lithified oolithic bauxites are abundant. The composition of these detrital textural elements differed slightly from that of the fine-grained matrix. They were mainly characterised by a very high content of Al-rich phases (boehmite and gibbsite). Generally, the matrix of these bauxites was composed of kaolinite and Al-rich phases. In some cases, the quasi-concentric structure of the ooids showed several internal discontinuities, suggesting that the accretion of the concentric layers was

interrupted several times by shorter or longer episodes of mechanical agitation (local transport). We propose that the tectonic deformation of the previously flat emerged area of the wedge top with ongoing bauxitization processes was the main cause of allochthony, that is, the redeposition of bauxite from the folded zone (hinge and limb area) to the synclinal depressions (Figure 12). Evidence of the replacement of boehmite with gibbsite was observed in the BSE images. Different processes or stages have been identified in the formation of these bauxites: the formation of pisolithic bauxite by intense weathering, fragmentation of the pisolithic bauxite and the formation of fragments and clasts, formation of pelitomorphic bauxite with kaolinite and Al-rich phases, and finally, crystallisation of gibbsite that cemented and replaced boehmite and other phases.

The embedded pelitomorphic matrix (reddish–russet or yellowish–red) is muddy and full of fine silt-sized (≤5–10 μm) extraclasts. In addition to allochthonous fragments, some Fe oxide-impregnated clasts and horizons also appeared. This could be attributed to the diagenetic redox processes, such as Fe mobilisation and reprecipitation, induced by the hydrological change of the oscillating groundwater table (depressions of the palaeorelief could have been under stagnant water). During the later stages of subaerial exposure, the circulating pore water solutions along the interface between the bauxite and karstic bedrock (foraminiferal or Upper Cretaceous limestones) or bauxite and the overlying Promina deposits could have precipitated calcite cement. The mosaic-like, non-luminescent sparry calcite suggested precipitation from freshwater. Embedded and coated previously formed stabilised ferric iron oxide minerals survived in a water-saturated environment. Samples from intensively faulted zones show "vague fluidal" structures and sepic plasmic fabric of the matrix (stress-induced orientation of clay-size components). Owing to the ductility of bauxite deposits in comparison with the basement and overlying carbonates, bauxites often pinch out at fault discontinuities. This indicated that these deposits were already formed before the intense Dinaric orogeny (Handy et al., 2015) and the deformation of the entire area (folded and thrust belts). However, the wetting and drying of the weathered material and slumping of the semi-lithified material could be excluded.

The differences in the mineralogical composition among the NDPGB bauxite deposits have already been observed in earlier works during the active exploitation (Sakač, 1972; Šinkovec et al., 1976; Sakač et al., 1993). In the new U-Pb data, the proportions of Palaeozoic, Cretaceous, and Palaeogene detrital zircon ages varied among the samples. The isolated Eocene age components of the deposits were also dissimilar. The possibility that some of the deposits were situated relatively close to each other did not collect volcanic ash from the same eruption was excluded. Thus, the only possibility remained was that the accumulation of material in the individual bauxite traps was diachronous.

A smaller share of the Palaeocene–Eocene zircon age components could have had the same origin as the tephra layers known from the Western Carpathian flysch (Botor et al., 2006). Less often, Upper Cretaceous zircons were possibly resedimented from previous Upper Cretaceous emersion phases on the AdCP (Figures 11A, B; Yuste et al., 2015; Carpatho–Balkan Banatite Belt/Apuseni–Banat–Timok–Srednogorie Belt; Neubauer, 2002; Gallhofer et al., 2015) or early alpine exhumation events (Plašienka et al., 2007). Older zircons, as well as epidote, muscovite, and quartz (Figure 3B), likely originated from the NE

ophiolitic hinterland, which was composed of different magmatic, metamorphic, and siliciclastic rocks (Pamić et al., 1998; Csontos et al., 2004; Schmid et al., 2008).

5.3 Preservation of bauxite deposits by the overlaying molasse

The long-term cooling trend, which culminated in the Eocene–Oligocene transition (EOT, ~34 Ma, Zachos et al., 1996; Houben et al., 2012; Kochhann et al., 2021; Costa et al., 2011), resulted in a gradual shift from a greenhouse to an icehouse climate. Global cooling was associated with waning volcanism, increased long-term organic carbon storage in the Paratethyan basins, increased silicate weathering in the collision zones, and a shift towards modern patterns of ocean currents with increased circulation and organic productivity (Allen and Armstrong, 2008).

The NDPGB bauxite deposits and eroded Rupelian palaeorelief soon became covered by a succession of the Promina Formation (initial molasse of the Dinaric orogeny). The characteristics of the initial layers of Promina largely depend on palaeorelief, ranging from brackish, lacustrine, and deltaic to shallow marine environments (Figures 11C, 11D, 11E). According to the calcareous nanoplanktons (*Isthmolithus rhenanus* Martini), Sakač et al. (1993) concluded that the younger part of Promina deposited belonged to the Early Oligocene. The selected euhedral zircon crystals from the BXH-4 sample (biocalcarenite from the Promina site, Figure 1) contained only Late Cretaceous, Permian, and older ages and not the Palaeogene U–Pb ages. As previously mentioned, the youngest detrital zircon age population from the NDPGB bauxites dates to approximately 34 Ma. All these age measurements suggested a transitional Priabonian–Rupelian MDA for the NDPGB bauxites and that the basal age of the youngest overlayed the sediments of the Promina molasse.

Soon after these events, sedimentation of the thick conglomerate bodies over the entire wider area was initiated (Figures 11E, 12C). In the Early-to-Middle Rupelian, abundant filling with Promina molasse deposits started at the proximal frontal part of the orogenic wedge (alluvial, lacustrine, deltaic, lagoonal, and carbonate shallow marine depositional environments; Babić et al., 1995). Until after the end of the Oligocene, the thickness of these (mostly conglomeratic) deposits reached 2 km, reflecting the erosion of the Mesozoic and Lower Eocene carbonates within the propagating Dinaric deformation system towards the foreland (Mamužić, 1975; Ivanović et al., 1978; Babić and Zupanič, 1983; 1988; 2008; 2012; Mrinjek, 1993a; 1993b; Zupanič and Babić, 2011; Mrinjek et al., 2012; Ćosović et al., 2018).

Present-day position of the exposed Lutetian–Priabonian NDPGB bauxite deposits indicate the possibility of the existence of a larger number of bauxite deposits (yet unknown or already eroded) along the contact of the Cretaceous–Eocene unconformity and the Oligocene molasse. Some were eroded during the later stages of the Dinaric orogeny, particularly in the hinge zones of the anticlinal forms (recently exposed Upper Cretaceous relief, Figure 1).

6 Conclusion

In summary, the following facts and results are highlighted:

1. The favourable climate conditions throughout the Eocene, as well as the karstified carbonate basement, provided excellent conditions for bauxitisation.
2. NDPGB karst bauxites showed a close relationship with other bauxites of the Tethyan (Mediterranean) realm.
3. Tectonic deformation of the area led to the partially *in situ* redeposition and accumulation of already bauxitised material.
4. The presence of rock fragments, along with broken and fragmented pisoids and clasts, suggests that the reworking processes caused the incorporation of fragments from a previous pisolitic bauxite into the younger pelitomorphic bauxite matrix.
5. Bauxite traps formed by tectonic deformation (formation of anticline hinges and syncline depressions) were subsequently covered, along the entire area, by Promina molasse, which helped preserve the thin, widely distributed, eroded, and redeposited bauxite masses.
6. The compositions of the investigated NDPGB bauxites (resolved using XRD, EDS, SEM, and whole-rock analyses) showed no genetic relationships with the calcareous Upper Cretaceous and Lower Eocene basements.
7. The presence of gibbsite, boehmite, kaolinite, Fe, and Ti oxides and the lack of quartz, carbonates, and only minor proportions of detrital smectites and illites suggest intense weathering during the formation of the analysed bauxites.
8. Based on the range between the detrital zircon age components (ca. 41 to ca. 34.5 Ma) and the overlying Promina sandstones, we substantially reduced the time span uncertainties of the subaerial exposure phase within the rather large stratigraphic gap between the Upper Cretaceous or Lower Eocene foraminiferal limestone palaeorelief and the overlying Promina molasse. Most of the detrital zircon crystals in the bauxite were derived from Eocene ashes of coeval explosive volcanism. Moreover, it was possible to isolate three major pulses at approximately 41, 38.5, and 34.5 Ma. However, we did not find traces of Palaeogene volcanic activity in the sandstone covering the Mount Promina bauxite deposit.
9. Zircon crystals from the Late Cretaceous magmatism were observed in all samples. Along with the grains of pre-Mesozoic U–Pb ages, they possibly represent aeolian material on the karstic surface or redeposited sediment from the flysch slivers of the emerging Dinarides.

Data availability statement

The original contributions presented in the study are included in the article/Supplementary Material; further inquiries can be directed to the corresponding author.

Author contributions

Conceptualisation: VB. Methodology: VB, ID, AM, MB, BB, IM, VK, EL, AY, PB, NT, HE, and AZ. Investigation: VB, ID, AM, MB, NT, DK, and SŠ. Visualization: VB. Funding acquisition: VB, MB, ID, HE, and BB. Writing—original draft: VB, PB, MB, and ID. Writing—review and editing: all authors. All authors contributed to the study with material preparation, data collection, and analysis. The first draft of the

manuscript was written by the first author, and all authors commented on all later versions of the manuscript. All authors contributed to the article and approved the submitted version.

Funding

Acknowledgments

Conflict of interest

Author SŠ was employed by INA-Industrija Nafte d.d.

The remaining authors declare that the research was conducted in the absence of any commercial or financial relationships that could be construed as a potential conflict of interest.

Publisher's note

Supplementary material

The Supplementary Material for this article can be found online at: https://www.frontiersin.org/articles/10.3389/feart.2023.1224164/full#supplementary-material

References

Alegret, L., Ortiz, S., Orue-etxebarria, X., Bernaola, G., Baceta, J. I., Monechi, S., et al. (2009). The paleocene–eocene thermal maximum: new data on microfossil turnover at the zumaia section, Spain. *Palaios* 24, 318–328. doi:10.2110/palo.2008.p08-057r

Aleva, G. J. J. (1994). *Laterites: Concepts, Geology, morphology and chemistry*. Wageningen, Netherlands: International Soil Reference and Information Centre, 169.

Allen, M. B., and Armstrong, H. A. (2008). Arabia-Eurasia collision and the forcing of midCenozoic global cooling. *Palaeogeogr. Palaeoclimatol. Palaeoecol.* 265, 52–58. doi:10.1016/j.palaeo.2008.04.021

Aydınçakır, E., Yücel, C., Ruffet, G., Gücer, M. A., Akaryalı, E., and Kaygusuz, A. (2022). Petrogenesis of post-collisional Middle Eocene volcanism in the Eastern Pontides (NE, Turkey): insights from geochemistry, whole-rock Sr-Nd-Pb isotopes, zircon U-Pb and ^{40}Ar-^{39}Ar geochronology. *Geochemistry* 82 (2), 125871. doi:10.1016/j.chemer.2022.125871

Babić, Lj., and Zupanič, J. (1988). Coarse-grained alluvium in the paleogene of northern dalmatia (Croatia, yugoslavia). *JAZU* 441 (23), 139–164.

Babić, Lj., and Zupanič, J. (2008). Evolution of a river-fed foreland basin fill: the North dalmatian flysch revisited (Eocene, outer Dinarides). *Nat. Croat.* 17, 357–374.

Babić, Lj., and Zupanič, J. (2012). Laterally variable development of a basin-wide transgressive unit of the North Dalmatian foreland basin (Eocene, Dinarides, Croatia). *Geol. Croat.* 65, 1–27. doi:10.4154/gc.2012.01

Babić, Lj., and Zupanič, J. (1983). "Paleogene clastic formations in northern Dalmatia," in *Contributions to Sedimentology of some carbonate and clastic units of the coastal Dinarides. Excursion guidebook*. Editors Lj. Babić and V. Jelaska (Split: International Association of Sedimentologists 4th Regional Meeting), 37–61.

Babić, Lj., and Zupanič, J. (1990). Progradacijski sljedovi u paleogenskom klastičnim bazenu Vanjskih Dinarida, od sjeverne Dalmacije do zapadne Hercegovine. *Rad. JAZU* 449 (24), 319–343.

Babić, Lj., and Zupanič, J. (2016). The youngest stage in the evolution of the dinaric carbonate platform: the upper nummulitic limestones in the North dalmatian foreland, middle Eocene, Croatia. *Nat. Croat.* 25/1, 55–71. doi:10.20302/nc.2016.25.3

Babić, L., Zupanić, J., and Kurtanjek, D. (1995). Sharply-topped alluvial gravel sheets in the Palaeogene Promina basin (Dinarides, Croatia). *Geol. Croat.* 48 (1), 33–48.

Bárdossy, G., and Aleva, G. J. J. (1990). *Lateritic bauxites. Developments in economic Geology*, 27. Amsterdam: Elsevier, 624.

Bárdossy, G., and Combes, P. J. (1999). Karst bauxites: interfingering of deposition and palaeoweathering. *Spec. Publ. Int. Assoc. Sedimentol.* 27, 189–206.

Bárdossy, G. (1982). *Karst Bauxites. Bauxite deposits on carbonate rocks*. Amsterdam: Elsevier.

Bárdossy, G., and Mindszenty, A. (2013). The iharkút bauxite. *Occas. Pap. Geol. Geophys. Inst. Hung.* 1, 133.

Bauluz, B., Yuste, A., Mayayo, M. J., and Canudo, J. I. (2014). Early kaolinization of detrital weald facies in the galve sub-basin (central iberian chain, north-east Spain) and its relationship to palaeoclimate. *Cretac. Res.* 50, 214–227. doi:10.1016/j.cretres.2014.03.014

Bogatyrev, B. A., Zhukov, V. V., and Tsekhovsky, Y. G. (2009). Formation conditions and regularities of the distribution of large and superlarge bauxite deposits. *Lithol. Min. Resour.* 44, 135–151. doi:10.1134/s0024490209020035

Bohaty, S. M., Zachos, J. C., Florindo, F., and Delaney, M. L. (2009). Coupled greenhouse warming and deep-sea acidification in the middle Eocene. *Paleoceanography* 24, 1–16. doi:10.1029/2008pa001676

Bohaty, S. M., and Zachos, J. C. (2003). Significant Southern Ocean warming event in the late middle Eocene. *Geology* 31, 1017. doi:10.1130/g19800.1

Boni, M., Reddy, S. M., Mondillo, N., Balassone, G., and Taylor, R. (2012). A distant magmatic source for Cretaceous karst bauxites of Southern Apennines (Italy), revealed through SHRIMP zircon age dating. *Terra nova.* 24, 326–332. doi:10.1111/j.1365-3121.2012.01068.x

Boni, M., Rollinson, G., Mondillo, N., Balassone, G., and Santoro, L. (2013). Quantitative mineralogical characterization of karst bauxite deposits in the Southern Apennines, Italy. *Econ. Geol.* 108, 813–833. doi:10.2113/econgeo.108.4.813

Botor, D., Dunkl, I., Rauch-Włodarska, M., and Eynatten, H. (2006). Attempt to dating of accretion in the west carpathian flysch belt: apatite fission track thermochronology of tuff layers. *GeoLines* 20, 21–23.

Boulange, B. (1984). *Les formations bauxitiques latériques de Côte d'Ivoire*. Paris: Travaux et Documents ORSTOM, 175.

Bralower, T. J., Zachos, J. C., Thomas, E., Parrow, M., Paull, C. K., Kelly, D. C., et al. (1995). Late Paleocene to Eocene paleoceanography of the equatorial pacific ocean: stable isotopes recorded at ocean drilling program site 865, allison guyot. *Paleoceanography* 10, 841–865. doi:10.1029/95pa01143

Brčić, V., Glumac, B., Brlek, M., Fuček, L., and Šparica Miko, M. (2021). Cenomanian-Turonian oceanic anoxic event (OAE2) imprint on the northwestern part of the Adriatic Carbonate Platform and a coeval intra-platform basin (Istria and Premuda Island, Croatia). *Cretac. Res.* 125, 104847. doi:10.1016/j.cretres.2021.104847

Brčić, V., Glumac, B., Fuček, L., Grizelj, A., Horvat, M., Posilović, H., et al. (2017). The cenomanian–turonian boundary in the northwestern part of the adriatic carbonate platform (ćićarija mtn., istria, Croatia): characteristics and implications. *Facies* 63, 17. doi:10.1007/s10347-017-0499-7

Brlek, M., Gaynor, S. P., Mongelli, G., Bauluz, B., Sinisi, R., Brčić, V., et al. (2021). Karst bauxite formation during miocene climatic optimum (central dalmatia, Croatia): mineralogical, compositional and geochronological perspectives. *Int. J. Earth Sci.* 110, 2899–2922. doi:10.1007/s00531-021-02091-z

Brlek, M., Tapster, S. R., Schindlbeck-Belo, J., Gaynor, S. P., Kutterolf, S., Hauff, F., et al. (2023). Tracing widespread Early Miocene ignimbrite eruptions and petrogenesis at the onset of the Carpathian-Pannonian Region silicic volcanism. *Gondwana Res.* 116, 40–60. doi:10.1016/j.gr.2022.12.015

Comer, J. B., Naeser, C. W., and McDowel, F. W. (1980a). Fission-track ages of zircon from Jamaican bauxite and Terra Rossa. *Econ. Geol.* 75, 117–121. doi:10.2113/gsecongeo.75.1.117

Ćosović, V., Balončić, D., Koić, M., Marjanac, T., Moro, A., Gušić, I., et al. (1994). Palaeontological evidence of Palaeogene transgression on Adriatic carbonate platform. *Géol. Méditerran.* 21 (3–4), 49–53. doi:10.3406/geolm.1994.1524

Ćosović, V., Drobne, K., and Moro, A. (2004). Paleoenvironmental model for Eocene foraminiferal limestones of the Adriatic carbonate platform (Istrian Peninsula). *Facies* 50, 61–75. doi:10.1007/s10347-004-0006-9

Ćosović, V., Mrinjek, E., Nemec, W., Spaniček, J., and Terzić, K. (2018). Development of transient carbonate ramps in an evolving foreland basin. *Basin Res.* 30, 746–765. doi:10.1111/bre.12274

Costa, E., Garcés, M., Sáez, A., Cabrera, L., and López-Blanco, M. (2011). The age of the "grande coupure" mammal turnover: new constraints from the eocene–oligocene record of the eastern ebro basin (NE Spain). *Palaeogeogr. Palaeoclimatol. Palaeoecol.* 301 (1–4), 97–107. doi:10.1016/j.palaeo.2011.01.005

Coxall, H. K., and Pearson, P. N. (2007). *Clim. Chang. Marrying signal from comput. Model. Biol. Proxies.* London, UK: The Micropalaeontological Society, Special Publications, The Geological Society, 351–387.The eocene-oligocene transition, deep time persepct

Csontos, L., Gerzina, N., Hrvatović, H., Schmid, S., and Tomljenović, B. (2004). *Structural evolution of the internal Dinarides: A preliminary study based on selected regions.* Thessaloniki, Greece: 5th International Symposium on Eastern Mediterranean Geology, 14–20.

D'Argenio, B., and Mindszenty, A. (1992). Tectonic and climatic control on apleokarst and baxuites. *G. Geol.* 54/1, 207–218.

Dal Piaz, G. V., Del Moro, A., Martin, S., and Venturelli, G. (1988). Post-collisional magmatism in the Ortler_Cevedale massif (northern Italy). *Jb. Geol.* 131, 533–551.

D'Argenio, B., and Mindszenty, A. (1995). Bauxites and related paleokarst: tectonic and climatic event markers at regional unconformities. *Eclog. Geol. Helv.* 88, 453–499.

D'Argenio, B., and Mindszenty, A. (1991). Karst bauxites at regional unconformities and geotectonic correlation in the Cretaceous of the Mediterranean. *Boll. della Soc. Geol. Ital.* 110/1, 85–92.

Davey, S. D., and Jenkyns, H. C. (1999). Carbon-isotope stratigraphy of shallow-water limestones and implications for the timing of Late Cretaceous sea-level rise and anoxic events (Cenomanian–Turonian of the peri-Adriatic carbonate platform, Croatia). *Eclogae Geol. Helvetiae* 92, 163–170.

Deady, É. A., Mouchos, E., Goodenough, K., Williamson, B. J., and Wall, F., 2016. A review of the potential for rare-earth element resources from European red muds: examples from Seydi̧ Sehir, Turkey and Parnassus-Giona, Greece. *Mineral. Mag.*, 80, 43–61. doi:10.1180/minmag.2016.080.052

Deady, É., Mouchos, E., Goodenough, K., Williamson, B., and Wall, F., 2014. Rare earth elements in karst-bauxites: A novel untapped European resource? ERES2014: 1st European rare earth resources conference, *Milos*, 04-07, .

Decelles, P. G., and Giles, K. A. (1996). Foreland basin systems. *Basin Res.* 8, 105–123. doi:10.1046/j.1365-2117.1996.01491.x

Déramond, J., Souquet, P., Fondecave-Wallez, M. J., and Specht, M. (1993). Relationships between thrust tectonics and sequence stratigraphy surfaces in foredeeps: model and examples from the pyrenees (Cretaceous-Eocene, France, Spain). *Geol. Soc. Lond. Special Publ.* 71, 193–219. doi:10.1144/gsl.sp.1993.071.01.09

Döbelin, N., and Kleeberg, R. (2015). *Profex*: A graphical user interface for the Rietveld refinement program*BGMN. J. Appl. Crystallogr.* 48, 1573–1580. doi:10.1107/s1600576715014685

Drobne, K., and Pavlovec, R. (1991). "Paleocene and Eocene beds in Slovenia and istria," in *Introduction to the paleogene SW Slovenia and istria. IGCP project 286 "early paleogene benthos", 2nd meeting postojna, paleontološki inštitut I.* Editors K. Drobne and R. Pavlovec (Ljubljana: Rakovca ZRC SAZU), 7–18.

Dunkl, I, Mikes, T., Simon, K., and von Eynatten, H., 2008. Brief introduction to the windows program pepita: data visualization, and reduction, outlier rejection, calculation of trace element ratios and concentrations from LA-ICP-MS data. In: *Laser ablation ICP-ms in the earth sciences: Current practices and outstanding issues. Mineralogical association of Canada, short course* (Ed. by P Sylvester) 40, 334–340.

Dunkl, I. (1992). Origin of eocene-covered karst bauxites of the transdanubian central range (Hungary): evidence for early Eocene volcanism. *Eur. J. Min.* 4, 581–596. doi:10.1127/ejm/4/3/0581

Erturk, M. A., Beyarslan, M., Chung, S.-L., and Lin, T.-H. (2018). Eocene magmatism (maden complex) in the southeast anatolian orogenic belt: magma genesis and tectonic implications. *Geosci. Front.* 9 (6), 1829–1847. doi:10.1016/j.gsf.2017.09.008

Estrade, G., Marquis, E., Smith, M., Goodenough, K., and Nason, P. (2019). REE concentration processes in ion adsorption deposits: evidence from the Ambohimirahavavy alkaline complex in Madagascar. *Ore Geol. Rev.* 112, 103027. doi:10.1016/j.oregeorev.2019.103027

Farics, E., Dunkl, I, Józsa, S., Haas, J., and Kovács, J., 2019. Traces of the late Eocene – early Oligocene volcanic activity in the buda hills (transdanubian range, Hungary): link to the volcanism along the periadriatic – mid-Hungarian – sava-vardar zone. *Geophys. Res. Abstr.* Vol. 21, EGU2019-3520.

Frei, D., and Gerdes, A. (2009). Precise and accurate *in situ* U-Pb dating of zircon with high sample throughput by automated LA-SF-ICP-MS. *Chem. Geol.* 261, 261–270. doi:10.1016/j.chemgeo.2008.07.025

Gain, S. E. M., Gréau, Y., Henry, H., Belousova, E., Dainis, I., Griffin, W. L., et al. (2019). Mud Tank zircon: long-term evaluation of a reference material for U-Pb dating, Hf-isotope analysis and trace element analysis. *Geostand. Geoanal. Res.* 43, 339–354. doi:10.1111/ggr.12265

Gallhofer, D., von Quadt, A., Peytcheva, I., Schmid, S. M., and Heinrich, C. A. (2015). Tectonic, magmatic, and metallogenic evolution of the Late Cretaceous arc in the Carpathian-Balkan orogen. *Tectonics* 34, 1813–1836. doi:10.1002/2015tc003834

Gehrels, G. (2014). Detrital zircon U-Pb geochronology applied to tectonics. *Annu. Rev. Earth Planet. Sci.* 42, 127–149. doi:10.1146/annurev-earth-050212-124012

Gibson, T. G., Bybell, L. M., and Mason, D. B. (2000). Stratigraphic and climatic implications of clay mineral changes around the Paleocene/Eocene boundary of the northeastern US margin. *Sediment. Geol.* 134, 65–92. doi:10.1016/s0037-0738(00)00014-2

Guynn, J., and Gehrels, G. E. (2010). *Comparison of detrital zircon age distributions in the K-S test.* Tucson: University of Arizona, Arizona Laser Chron Center, 16.

Handy, M. R., Ustaszewski, K., and Kissling, E. (2015). Reconstructing the Alps-Carpathians-Dinarides as a key to understanding switches in subduction polarity, slab gaps and surface motion. *Int. J. Earth. Sci.* 104 (1), 1–26. doi:10.1007/s00531-014-1060-3

Herriott, T. M., Crowley, J. L., Schmitz, M. D., Wartes, M. A., and Gillis, R. J. (2019). *Exploring the law of detrital zircon: LA-ICP MS and CA-TIMS geochronology of jurassic forearc strata*, 47. Alaska, USA: Cook Inlet, 1044–1048.

Houben, A. J. P., van Mourik, C. A., Montanari, A., Coccioni, R., and Brinkhuis, H. (2012). The Eocene–Oligocene transition: changes in sea level, temperature or both? *Palaeogeogr. Palaeoclimatol. Palaeoecol.* 335–336, 75–83. doi:10.1016/j.palaeo.2011.04.008

Hutchinson, D. K., Coxall, H. K., Lunt, D. J., Steinthorsdottir, M., de Boer, A. M., Baatsen, M., et al. (2021). The eocene–oligocene transition: A review of marine and terrestrial proxy data, models and model–data comparisons. *Clim. Past.* 17, 269–315. doi:10.5194/cp-17-269-2021

Ilijanić, N., Kovačević Galović, E., Gizdavec, N., Ivkić Filipović, I., Miko, S., and Peh, Z. (2023). Geochemical records in subaerial exposure environments in Croatia using discriminant function analysis of bauxite data. *Front. Earth Sci.* v10. doi:10.3389/feart.2022.1055435

Iqbal, S., Bibi, M., and Wagreich, M. (2023). Geochemistry of the triassic–jurassic lateritic bauxites of the salt range: implications for eastward extension of the tethyan bauxite deposits into Pakistan. *Int. J. Earth Sci.* 112, 1527–1552. doi:10.1007/s00531-023-02310-9

Ivanović, A., Sakač, K., Marković, S., Sokač, B., Šušnjar, M., Nikler, L., et al. (1973). *Osnovna geološka karta SFRJ 1:100000, list obrovac [basic geological map of SFRY 1:100000, obrovac sheet – in Croatian]. Geološki zavod, zagreb.* Beograd: Savezni geološki zavod.

Ivanović, A., Sakač, K., Sokač, B., Vrsalović-Carević, I., and Zupanič, J. (1976). *Osnovna geološka karta SFRJ 1:100 000: Tumač za list Obrovac.* Beograd: Savezni geoloski zavod, 61. [In Croatian, with English summary.

Ivanović, A., Sikirica, V., Marković, S., and Sakač, K. (1977). *Osnovna geološka karta SFRJ 1:100000, list drniš [basic geological map of SFRY 1:100000, drniš sheet – in Croatian]. Geološki zavod, zagreb.* Beograd: Savezni geološki zavod.

Ivanović, A., Sikirica, V., and Sakač, K. (1978). *Osnova geološka karta SFRJ 1:100 000: Tumač za list Drniš.* Beograd: Savezni geoloski zavod, 59. [In Croatian, with English summary.

Jackson, S., Pearson, N., Griffin, W., and Belousova, E. (2004). The application of laser ablationinductively coupled plasma-mass spectrometry to *in situ* U-Pb zircon geochronology. *Chem. Geol.* 211, 47–69. doi:10.1016/j.chemgeo.2004.06.017

Jenkyns, H. C. (1991). Impact on cretaceous sea level rise and anoxic events on the Mesozoic carbonate platform of Yugoslavia. *Am. Asso. Pet. Geol. Bull.* 75 (6), 1007–1017.

Ji, W.-Q., Malusà, M. G., Tiepolo, M., Langone, A., Zhao, L., and Wu, F.-Y. (2019). Synchronous periadriatic magmatism in the western and central Alps in the absence of slab breakoff. *Terra nova.* 31, 120–128. doi:10.1111/ter.12377

Jovane, L., Sprovieri, M., Florindo, F., Acton, G., Coccioni, R., Dall'Antonia, B., et al. (2007). Eocene-Oligocene paleoceanographic changes in the stratotype section, Massignano, Italy: clues from rock magnetism and stable isotopes. *J. Geophys. Res.* 112, B11101. doi:10.1029/2007jb004963

Karadağ, M. M., Küpeli, S., Arýk, F., Ayhan, A., Zedef, V., and Döyen, A. (2009). Rare earth element (REE) geochemistry and genetic implications of the Mortaş bauxite deposit (Seydişehir/Konya – southern Turkey). *Geochemistry* 69 (2), 143–159. doi:10.1016/j.chemer.2008.04.005

Kázmér, M., Dunkl, I., Frisch, W., Kuhlemann, J., and Ozsvárt, P. (2003). The Palaeogene forearc basin of the eastern Alps and the western carpathians: subduction erosion and basin evolution. *J. Geol. Soc.* 160, 413–428.

Kelemen, P., Dunkl, I., Csillag, G., Mindszenty, A., Józsa, S., Fodor, L., et al. (2023). Origin, timing and paleogeographic implications of Paleogene karst bauxites in the northern Transdanubian range, Hungary. *Int. J. Earth Sci.* 112, 243–264. doi:10.1007/s00531-022-02249-3

Kender, S., Bogus, K., Pedersen, G. K., Dybkjær, K., Mather, T. A., Mariani, E., et al. (2021). Paleocene/Eocene carbon feedbacks triggered by volcanic activity. *Nat. Commun.* 12, 5186. doi:10.1038/s41467-021-25536-0

Kennedy, A., Wotzlaw, J.-F., Crowley, J., Schmitz, M., and Schaltegger, U. (2014). Eocene zircon reference material for microanalysis of U-Th-Pb isotopes and trace elements. *Can. Mineralogist* 52, 409–421. doi:10.3749/canmin.52.3.409

Kennett, J. P., and Stott, L. D. (1991). Abrupt deep-seawarming, palaeoceanographic changes and benthic extinctions at the end of the Palaeocene. *Nature* 353, 225–229. doi:10.1038/353225a0

Khomsi, S., de Lamotte, D. F., Bédir, M., and Oussema, E. (2016). The late Eocene and late miocene fronts of the atlas belt in eastern maghreb: integration in the geodynamic evolution of the mediterranean domain. *Arab. J. Geosci.* 9, 650. doi:10.1007/s12517-016-2609-1

Khosravi, M., Abedini, A., Alipour, S., and Mongelli, G. (2017). The darzi-vali bauxite deposit, west-azarbaidjan province, Iran: critical metals distribution and parental affinities. *J. Afr. Earth. Sci.* 129, 960–972. doi:10.1016/j.jafrearsci.2017.02.024

Koch, P. L., Zachos, J. C., and Gingerich, P. D. (1992). Correlation between isotope records in marine and continental carbon reservoirs near the Palaeocene/Eocene boundary. *Nature* 358, 319–322. doi:10.1038/358319a0

Kochhann, M. V. L., Savian, J. F., Tori, F., Catanzariti, R., Coccioni, R., Frontalini, F., et al. (2021). Orbital tuning for the middle Eocene to early Oligocene monte cagnero section (Central Italy): paleoenvironmental and paleoclimatic implications. *Palaeogeogr. Palaeoclimatol. Palaeoecol.* 577, 110563. doi:10.1016/j.palaeo.2021.110563

Korbar, T., Glumac, B., Cvetko-Tešović, B., and Cadieux, S. B. (2012). Response of a carbonate platform to the cenomanian–turonian drowning and OAE 2: A case study from the adriatic platform (dalmatia, Croatia). *J. Sediment. Res.* 82, 163–176. doi:10.2110/jsr.2012/17

Korbar, T. (2009). Orogenic evolution of the external Dinarides in the NE adriatic region: A model constrained by tectonostratigraphy of upper cretaceous to paleogene carbonates. *Earth-Science Rev.* 96, 296–312. doi:10.1016/j.earscirev.2009.07.004

Krippner, A., and Bahlburg, H. (2012). Provenance of pleistocene rhine river middle terrace sands between the Swiss–German border and cologne based on U–Pb detrital zircon ages. *Int. J. Earth Sci.* 102, 917–932. doi:10.1007/s00531-012-0842-8

Lear, C. H., Rosenthal, Y., Coxall, H. K., and Wilson, P. A. (2004). Late Eocene to early Miocene ice sheet dynamics and the global carbon cycle. *Paleoceanography* 19, 4015. doi:10.1029/2004pa001039

Ludwig, K. R. (2012). *User's manual for Isoplot 3.75: A geochronological toolkit for microsoft excel*, 4. China: Berkeley Geochronology Center Special Publication, 70., no.

Lustrino, M., Morra, V., Fedele, L., and Franciosi, L. (2009). Beginning of the Apennine subduction system in central western Mediterranean: constraints from Cenozoic "orogenic" magmatic activity of Sardinia, Italy. *Tectonics* 28, TC5016. doi:10.1029/2008tc002419

Maksimovic, Z. (1968). Distribution of trace elements in bauxite deposits of Hercegovina, Yugoslavia. *Trav. ICSOBA* 5, 31–36.

Maksimović, Z., and Pantó, G., 1978. Minerals of the rare-earth elements in karstic bauxites: synchysite-(Nd), a new mineral from grebnik deposit. *4ᵗʰ International Congress, ICSOBA, International Committee for Study of Bauxite, Alumina & Aluminium*, Athens, Greece pp. 540–552.

Maksimović, Z. (1976). "Trace elements in some Yugoslav bauxite deposits and their significance," in *Proc. IV Jugosl. Symp. on exploration of bauxites* (Herceg Novi, 29–33.

Mamužić, P. (1975). *Osnovna geološka karta SFRJ 1:100 000: Tumač za List Šibenik*. Beograd: Savezni geološki zavod, 37. [In Croatian, with English summary.

Mamužić, P. (1971). *Osnovna geološka karta SFRJ 1:100000, list Šibenik [Basic Geological Map of SFRY 1:100000, Šibenik sheet – in Croatian]. Geološki zavod, Zagreb.* Beograd: Savezni geološki zavod.

Marchand, E., Séranne, M., Bruguier, O., and Vinches, M. (2021). LA-ICP-MS dating of detrital zircon grains from the Cretaceous allochthonous bauxites of Languedoc

(south of France): provenance and geodynamic consequences. *Basin Res.* 33, 270–290. doi:10.1111/bre.12465

Marchev, P., Georgiev, S., Raicheva, R., Peytcheva, I., Albrecht, Q., Ovtcharova, M., et al. (2013). Adakitic magmatism in post-collisional setting: an example from the early–middle Eocene magmatic belt in southern Bulgaria and northern Greece. *Lithos* 180–181, 159–180. doi:10.1016/j.lithos.2013.08.024

McDonough, W. F., and Sun, S. S. (1995). The composition of the Earth. *Chem. Geol.* 67, 223–253. doi:10.1016/0009-2541(94)00140-4

McInherney, F. A., and Wing, S. (2011). The paleocene-eocene thermal maximum: A perturbation of carbon cycle, climate, and biosphere with implications for the future. *Annu. Rev. Earth Planet. Sci.* 39, 489–516. doi:10.1146/annurev-earth-040610-133431

McQuarrie, N., Stock, J. M., Verdel, C., and Wernicke, B. (2003). Cenozoic evolution of Neotethys and implications for the causes of plate motions. *Geophys. Res. Lett.* 30. doi:10.1029/2003gl017992

Metcalfe, I. (2021). Multiple Tethyan ocean basins and orogenic belts in Asia. *Gondwana Res.* 100, 87–130. doi:10.1016/j.gr.2021.01.012

Mindszenty, A. (2016). Bauxites: feedbacks of system earth at greenhouse times. *Geol. Croat.* 69, 79–87. doi:10.4154/gc.2016.07

Mondillo, N., Boni, M., Balassone, G., and Rollinson, G. (2011). Karst bauxites in the campania apennines (southern Italy): A new approach. *Period. Di Mineral.* 80, 407–432.

Mongelli, G., Boni, M., Buccione, R., and Sinisi, R. (2014). Geochemistry of the apulian karst bauxites (southern Italy): chemical fractionation and parental affinities. *Ore. Geol. Rev.* 63, 9–21. doi:10.1016/j.oregeorev.2014.04.012

Mongelli, G., Boni, M., Oggiano, G., Mameli, P., Sinisi, R., Buccione, R., et al. (2017). Critical metals distribution in tethyan karst bauxite: the cretaceous Italian ores. *Ore. Geol. Rev.* 86, 526–536. doi:10.1016/j.oregeorev.2017.03.017

Mongelli, G., Buccione, R., Gueguen, E., Langone, A., and Sinisi, R. (2016). Geochemistry of the apulian allochthonous karst bauxite, southern Italy: distribution of critical elements and constraints on late cretaceous peri-tethyan palaeogeography. *Ore. Geol. Rev.* 77, 246–259. doi:10.1016/j.oregeorev.2016.03.002

Mrinjek, E. (1993a). Conglomerate fabric and paleocurrent measurment in the braided fluvial system of the Promina Beds in northern Dalmatia (Croatia). *Geol. Croat.* 46/1, 125–136.

Mrinjek, E., Nemec, W., Pecinger, V., Mikša, G., Vlahović, I., Ćosović, V., et al. (2012). The eocene-oligocene Promina beds of the dinaric Foreland Basin in northern dalmatia. *J. Alp. Geol.* 55, 409–451.

Mrinjek, E. (1993b). Sedimentology and depositional setting of alluvial Promina Beds in northern Dalmatia, Croatia. *Geol. Croat.* 46/2, 243–261.

Neubauer, F. (2002). Contrasting late cretaceous with neogene ore provinces in the alpine-balkan-carpathian-dinaride collision belt. *Geol. Soc. Lond. Spec. Publ.* 204, 81–102. doi:10.1144/gsl.sp.2002.204.01.06

Ori, G. G., and Friend, P. F. (1984). Sedimentary basins formed and carried piggyback on active thrust sheets. *Geology* 12, 475–478. doi:10.1130/0091-7613(1984)12<475:sbfacp>2.0.co;2

Otoničar, B. (2007). Upper cretaceous to paleogene forebulge unconformity associated with foreland basin evolution (kras, matarsko podolje and istria; SW Slovenia and NW Croatia). *Acta Carsologica* 36/1, 101–120.

Özlü, N. (1983). Trace-element content of "karst bauxites" and their parent rocks in the mediterranean belt. *Mineral. Deposita* 18, 469–476. doi:10.1007/bf00204491

Paces, J. B., and Miller, J. D. (1993). Precise U-Pb ages of Duluth Complex and related mafic intrusions, northeastern Minnesota: geochronological insights to physical, petrogenetic, paleomagnetic, and tectonomagmatic processes associated with the 1.1 Ga Midcontinent Rift System. *J. Geophys. Res.* 98, 13997–14013. doi:10.1029/93jb01159

Pamić, J., Balen, D., and Herak, M. (2002). Origin and geodynamic evolution of Late Paleogene magmatic associations along the Periadriatic-Sava-Vardar magmatic belt. *Geodinarnica Acta* 15, 209–231. doi:10.1016/s0985-3111(02)01089-6

Pamić, J., Gušić, I., and Jelaska, V. (1998). Geodynamic evolution of the central Dinarides. *Tectonophysics* 297 (1–4), 251–268. doi:10.1016/s0040-1951(98)00171-1

Petrinjak, K., Budić, M., Bergant, S., and Korbar, T. (2021). Megabeds in Istrian Flysch as markers of synsedimentary tectonics within the Dinaric foredeep (Croatia). *Geol. Croat.* 74/2, 99–120. doi:10.4154/gc.2021.07

Plašienka, D., Broska, I., Kissová, D., and Dunkl, I. (2007). Zircon fission-track dating of granites from the vepor-gemer belt (western carpathians): constraints for the early alpine exhumation history. *J. Geosciences* 52 (1–2), 113–123. doi:10.3190/jgeosci.009

Radusinović, S., and Papadopoulos, A. (2021). The potential for REE and associated critical metals in karstic bauxites and bauxite residue of Montenegro. *Minerals* 11, 975. doi:10.3390/min11090975

Retallack, G. J. (2008). Cool-climate or warm-spike lateritic bauxites at high latitudes? *J. Geol.* 116, 558–570. doi:10.1086/592387

Retallack, G. J. (2009). Greenhouse crises of the past 300 million years. *Geol. Soc. Am. Bull.* 121, 1441–1455. doi:10.1130/b26341.1

Retallack, G. J. (2010). Lateritization and bauxitization events. *Econ. Geol.* 105, 655–667. doi:10.2113/gsecongeo.105.3.655

Sakač, K. (1972)., 17/73. Zagreb, 221–223.A new survey of stratigraphic position of bauxite-bearing horizons in Croatia (Yugoslavia)*Bull. Sci. Cons. Acad. Yougosl. A*

Sakač, K. (1960). Geološka građa i boksitne pojave područja Novigrad–Obrovac u sjevernoj Dalmaciji. *Geol. Vijes.* 14, 323–345. [In Croatian, with German summary.

Sakač, K. (1969). Linhas críticas integrada na biblioteca virtual de Educação. *Geol. Vijes.* 23, 163–164. doi:10.26512/lc.v12i23.3295

Sakač, K., Šinkovec, B., Durn, G., and Benić, J. (1993). The bauxites and jelar-beds. *Rudarsko-geološko-naftni Zb.* 5, 59–64.

Sakač, K., and Šinkovec, B. (1991). The bauxites of the Dinarides. *Trav. ICSOBA 20–21*, 1–12.

Schellmann, W. (1994). Geochemical differentiation in laterite and bauxite formation. *CATENA* 21 (Issues 2–3), 131–143. doi:10.1016/0341-8162(94)90007-8

Schmid, S. M., Bernoulli, D., Fügenschuh, B., Matenco, L., Schefer, S., Schuster, R., et al. (2008). The alpine-carpathian-dinaridic orogenic system: correlation and evolution of tectonic units. *Swiss J. Geosciences* 101, 139–183. doi:10.1007/s00015-008-1247-3

Schmid, S. M., Fügenschuh, B., Kounov, M., Matenco, L., Nievergelt, P., Oberhänsli, R., et al. (2020). Tectonic units of the Alpine collision zone between Eastern Alps and western Turkey. *Gondwana Res.* 78, 308–374. doi:10.1016/j.gr.2019.07.005

Scotese, C., 2014. *Atlas of paleogene paleogeographic maps (mollweide projection)*,Maps 8-15, Vol. 1, The Cenozoic, PALEOMAP Atlas for ArcGIS, PALEOMAP Project, Evanston, IL.

Shackleton, N. J., and Kennett, J. P., 1975. Paleotemperature history of the Cenozoic and the initiation of Antarctic glaciation: oxygen and carbon isotope analyses in DSDP Sites 277, 281: *Initial Rep. Deep Sea Drill. Proj.*, Vol. 29: Washington, D.C., Government Printing Office, 743–755.

Sharman, G. R., and Malkowski, M. A. (2020). Needles in a haystack: detrital zircon U-Pb ages and the maximum depositional age of modern global sediment. *Earth-Science Rev.* 203, 103109–109. doi:10.1016/j.earscirev.2020.103109

Sinisi, R. (2018). Mineralogical and geochemical features of cretaceous bauxite from san giovanni rotondo (apulia, southern Italy): A provenance tool. *Minerals* 8, 567. doi:10.3390/min8120567

Šinkovec, B., Sakač, K., and Šušnjara, A. (1976). Lower cretaceous bauxites of the kijevo area and Mt. Dinara, dalmatia (southern Croatia). *Geološki Vijesn.* 29, 277–285.

Sláma, J., Košler, J., Condon, D. J., Crowley, J. L., Gerdes, A., Hanchar, J. M., et al. (2008). Plešovice zircon — a new natural reference material for U–Pb and Hf isotopic microanalysis. *Chem. Geol.* 249, 1–35. doi:10.1016/j.chemgeo.2007.11.005

Smith, V. C., Isaia, R., Engwell, S. L., and Albert, P. G. (2016). Tephra dispersal during the campanian ignimbrite (Italy) eruption: implications for ultra-distal ash transport during the large caldera-forming eruption. *Bull. Volcanol.* 78, 45. doi:10.1007/s00445-016-1037-0

Španiček, J., Ćosović, V., Mrinjek, E., and Vlahović, I. (2017). Early Eocene evolution of carbonate depositional environments recorded in the čikola canyon (North Dalmatian Foreland Basin, Croatia). *Geol. Croat.* 70/1, 11–25. doi:10.4154/gc.2017.05

Spencer, C. J., Kirkland, C. L., and Taylor, R. J. M. (2016). Strategies towards statistically robust interpretations of *in situ* U–Pb zircon geochronology. *Geosci. Front.* 7 (4), 581–589. doi:10.1016/j.gsf.2015.11.006

Stampfli, G. M., 2005. Plate tectonics of the Apulia-Adria microcontinents. In: *CROP project: Deep seismic exploration of the central mediterranean and Italy* (Ed. by J. R. Finetti), pp. 747–766. Elsevier, Amsterdam.

Stoops, G., Marcelino, V., and Mees, F. (2010). *Interpretation of micromorphological features of soils and regoliths*. China: Elsevier, 720.

Storey, M., Duncan, R. A., and Swisher, C. C. (2007). Paleocene-eocene thermal maximum and the opening of the northeast atlantic. *Science* 316, 587–589. doi:10.1126/science.1135274

Šušnjara, A., and Šćavničar, B. (1978). "Heavy minerals as provenance indices of tertiary bauxites in Dalmatia (Yugoslavia)," in *4th international congress for the study of bauxites, alumina and aluminium ICSOBA 2* (Athens, 822–837.

Tardy, Y., Kobilsek, B., and Paquet, H. (1991). Mineralogical composition and geographical distribution of African and Brazilian periatlantic laterites. The influence of continental drift and tropical paleoclimates during the past 150 million years and implications for India and Australia. *J. Afr. Earth Sci.* 12 (1/2), 283–295. doi:10.1016/0899-5362(91)90077-c, No.

Tari, V., 2002. Evolution of the northern and western Dinarides: A tectonostratigraphic approach. In: *Continental collision and the tectono-sedimentary evolution of forelands* (Ed. By G. Bertotti, K. Schulmann, and S. A. P. L. Cloetingh) China, EGU Stephan Mueller Spec. Publ., 1, 223–236.

Taylor, S. R., and McLennan, S. M. (1985). *The continental crust: Its composition and evolution*. Oxford: Blackwell, 1–312.

Thomas, E., and Shackleton, N. J. (1996). "The latest Paleocene benthic foraminiferal extinction and stable isotope anomalies," in *Correlation of the early paleogene in northwest Europe*. Editors R. O. Knox, R. M. Corfield, and R. E. Dunay, 101, 401–441.*Geol. Soc. Spec. Publ.*

Tišljar, J., Vlahović, I., Velić, I., and Sokač, B. (2002). Carbonate platform megafacies of the jurassic and cretaceous deposits of the karst Dinarides. *Geol. Croat.* 55/2, 139–170. doi:10.4154/gc.2002.14

Tomašić, N., Čobić, A., Bedeković, M., Miko, S., Ilijanić, N., Gizdavec, N., et al. (2021). Rare earth elements enrichment in the upper Eocene tošići-dujići bauxite deposit, Croatia, and relation to REE mineralogy, parent material and weathering pattern. *Minerals* 11, 1260. doi:10.3390/min11111260

Utescher, T., and Mosbrugger, V. (2007). Eocene vegetation patterns reconstructed from plant diversity - a global perspective. *Palaeogeogr. Palaeoclimatol. Palaeoecol.* 247 (Issues 3–4), 243–271. doi:10.1016/j.palaeo.2006.10.022

Valeton, I. (1994). Element concentration and formation of ore deposits by weathering. *Catena* 21, 99–129. doi:10.1016/0341-8162(94)90006-x

Valeton, I. (1991). Processes of allochthony and autochthony in bauxites of carbonate platforms of the Mediterranean area. *Mineral. Wealth* 71, 13–28.

Van Couvering, J. A., Aubry, M. P., Berggren, W. A., Bujak, J. P., Naeser, C. W., and Wieser, T. (1981). The terminal Eocene event and the Polish connection. *Palaeo Palaeo Palaeo* 36, 321–362. doi:10.1016/0031-0182(81)90111-5

Van der Boon, A., Kuiper, K. F., van der Ploeg, R., Cramwinckel, M. J., Honarmand, M., Sluijs, A., et al. (2021). Exploring a link between the middle Eocene climatic optimum and neotethys continental arc flare-up. *Clim. Past.* 17, 229–239. doi:10.5194/cp-17-229-2021

Van Unen, M., Matenco, L., Nader, F. H., Darnault, R., Mandic, O., and Demir, V. (2019). Kinematics of foreland-vergent crustal accretion: inferences from the Dinarides evolution. *Tectonics* 38, 49–76. doi:10.1029/2018tc005066

Velić, I., Tišljar, J., Vlahović, I., Matičec, D., and Bergant, S., 2003. Evolution of the istrian part of the adriatic carbonate platform from the middle jurassic to the santonian and formation of the flysch basin during the Eocene: main events and regional comparison. Field trip guidebook. In: 22nd *IAS meeting of Sedimentology, opatija, 17–19 september*, Zagreb, p 3–18.

Velić, I., Tišljar, J., Vlahović, I., Matičec, D., Korbar, T., Moro, A., et al. (2002b). "Geological evolution of istria (NW part of the adriatic carbonate platform, Croatia)," in *6th international congress on rudists, rovinj. Abstracts and excursion guidebook*. Editors I. Vlahović and T. Korbar (Zagreb, 83–93).

Velić, I., and Vlahović, I. (2009). *Explanatory text for geologic map of Croatia 1: 300.000*. Zagreb: Croatian Geological Survey.

Velić, I., Vlahović, I., and Matičec, D. (2002a). Depositional sequences and palaeogeography of the Adriatic carbonate platform. *Mem. Soc. Geol. It.* 57, 141–151.

Vermeesch, P. (2018). IsoplotR: A free and open toolbox for geochronology. *Geosci. Front.* 9, 1479–1493. doi:10.1016/j.gsf.2018.04.001

Vermeesch, P. (2012). On the visualisation of detrital age distributions. *Chem. Geol.* 312–313, 190–194. doi:10.1016/j.chemgeo.2012.04.021

Vlahović, I., Tišljar, J., Velić, I., and Matičec, D. (2005). Evolution of the adriatic carbonate platform: palaeogeography, main events and depositional dynamics. *Paleogeogr. Paleoclimatol. Paleoecol.* 220, 333–360. doi:10.1016/j.palaeo.2005.01.011

Westerhold, T., Marwan, N., Drury, A. J., Liebrand, D., Agnini, C., Anagnostou, E., et al. (2020). An astronomically dated record of Earth's climate and its predictability over the last 66 million years. *Sci. (80-.)* 369, 1383–1387. doi:10.1126/science.aba6853

Wiedenbeck, M., Allé, P., Corfu, F., Griffin, W. L., Meier, M., Oberli, F., et al. (1995). Three natural zircon standards for U–Th–Pb, Lu–Hf, trace element and REE analyses. *Geostand. Newsletters* 19, 1–23. doi:10.1111/j.1751-908x.1995.tb00147.x

Yang, S., Wang, Q., Liu, X., Kan, Z., Santosh, M., and Deng, J. (2022). Global spatio-temporal variations and metallogenic diversity of karst bauxites and their tectonic, paleogeographic and paleoclimatic relationship with the Tethyan realm evolution. *Earth-Science Rev.* 233, 104184. doi:10.1016/j.earscirev.2022.104184

Yuste, A., Bauluz, B., and Mayayo, M. J. (2015). Genesis and mineral transformations in lower cretaceous karst bauxites (NE Spain): climatic influence and superimposed processes. *Geol. J.* 50, 839–857. doi:10.1002/gj.2604

Zachos, J. C., Lohmann, K. C., Walker, J. C. G., and Wise, S. W., Jr. (1993). Abrupt climate change and transient climates during the paleogene: A marine perspective. *J. Geol.* 101, 191–213. doi:10.1086/648216

Zachos, J. C., Pagani, M., Sloan, L., Thomas, E., and Billups, K. (2001). Trends, rhythms, and aberrations in global climate 65 Ma to present. *Science* 292, 686–693. doi:10.1126/science.1059412

Zachos, J. C., Quinn, T. M., and Salamy, K. A. (1996). High-resolution (104 years) deep-sea foraminiferal stable isotope records of the Eocene-Oligocene climate transition. *Paleoceanography* 11, 251–266. doi:10.1029/96pa00571

Zamagni, J., Mutti, M., and Košir, A. (2008). Evolution of shallow benthic communities during the late paleocene-earliest Eocene transition in the northern tethys (SW Slovenia). *Facies* 54, 25–43. doi:10.1007/s10347-007-0123-3

Zupanič, J., and Babić, Lj. (2011). Sedimentary evolution of an inner foreland basin margin: paleogene Promina Beds of the type area, Mt. Promina (Dinarides, Croatia). *Geol. Croat.* 64/2, 101–119. doi:10.4154/gc.2011.09